Exocrine gland-resident memory CD8$^+$ T cells use mechanosensing for tissue surveillance

Nora Ruef[1,*], Jose Martínez Magdaleno[1,*], Xenia Ficht[2], Vladimir Purvanov[3], Matthieu Palayret[1], Stefanie Wissmann[1], Petra Pfenninger[1], Bettina Stolp[4], Flavian Thelen[5], Juliana Barreto de Albuquerque[6], Philipp Germann[7], James Sharpe[7,8,9], Jun Abe[1], Daniel F. Legler[3,10,11], Jens V. Stein[1,**]

[1] Department of Oncology, Microbiology and Immunology, University of Fribourg, 1700 Fribourg, Switzerland

[2] Department of Biosystems Science and Engineering, ETH Zürich Mattenstrasse 22, 4058, Basel, Switzerland

[3] Biotechnology Institute Thurgau (BITg) at the University of Konstanz, 8280 Kreuzlingen, Switzerland

[4] Department for Infectious Diseases, Integrative Virology, Center for Integrative Infectious Disease Research, University Hospital Heidelberg, 69120 Heidelberg, Germany

[5] Department of Medical Oncology and Hematology, University of Zürich and University Hospital Zürich, 8091 Zürich, Switzerland

[6] Division of Experimental Pathology, Institute of Pathology, University of Bern, 3008 Bern, Switzerland

[7] Centre for Genomic Regulation (CRG), Barcelona Institute of Science and Technology (BIST), 08003 Barcelona, Spain

[8] European Molecular Biology Laboratory (EMBL) Barcelona, 08003 Barcelona, Spain

[9] Institucio' Catalana de Recerca i Estudis Avancats (ICREA), 08010 Barcelona, Spain

[10] Faculty of Biology, University of Konstanz, 78464 Konstanz, Germany

[11] Theodor Kocher Institute, University of Bern, 3011 Bern, Switzerland

* Equal contribution

** To whom correspondence should be addressed

Contact: Jens V. Stein

Department of Oncology, Microbiology and Immunology
University of Fribourg
Ch. du Musée 5
CH-1700 Fribourg
email: jens.stein@unifr.ch

Abstract

Tissue-resident $CD8^+$ T cells (T_{RM}) constitutively scan peptide-MHC (pMHC) in their organ of residence to intercept microbial spread. Recent data showed that T_{RM} lodged in exocrine glands perform tissue scanning in the absence of any chemoattractant or adhesion receptor signaling, thus bypassing the requirement for canonical migration-promoting factors. The signals eliciting this non-canonical motility mode and its relevance for organ surveillance have remained unknown. Using mouse models of viral infections, we report that exocrine gland T_{RM} autonomously generated front-to-back F-actin flow for locomotion, accompanied by high cortical actomyosin contractility and leading edge bleb formation. The distinctive mode of exocrine gland T_{RM} locomotion was triggered by sensing physical confinement, and closely correlated with nuclear deformation, which acts as a mechanosensor via an arachidonic acid and Ca^{2+}-signaling pathway. In contrast, naïve $CD8^+$ T cells or T_{RM} surveilling microbe-exposed epithelial barriers did not show mechanosensing capacity. Inhibition of nuclear mechanosensing disrupted exocrine gland T_{RM} scanning and impaired their ability to intercept target cells. In sum, confinement suffices to elicit autonomous T cell surveillance in glands with restricted chemokine expression, and constitutes a complementary scanning strategy to chemosensing-dependent migration.

Introduction

$CD8^+$ T cell-mediated protection against viral infections hinges on the rapid detection of cognate pMHC presented on antigen-presenting and infected host cells. To expedite this process, $CD8^+$ T cells integrate biochemical cues of their microenvironment via chemoattractant and adhesion receptors *(1)*. During the course of an immune response, $CD8^+$ T cells adapt their adhesion and chemoattractant receptor expression pattern to their differentiation status. These expression patterns enable clonal selection in lymphoid organs, followed by elimination of infected cells in inflamed tissue and tissue surveillance in the memory phase *(2)*. More specifically, naïve and central memory $CD8^+$ T cells (T_N and T_{CM}, respectively) express CD62L and CCR7 for homing to secondary lymphoid organs (SLO), while effector and effector memory T cells (T_{EFF} and T_{EM}, respectively) display high surface levels of inflammatory chemokine and adhesion receptors to enter non-lymphoid tissues. Chemokine and adhesion receptors are also critical for interstitial scanning within target organs, the prerequisite for antigen-specific protection afforded by T_{EFF} *(3–5)*. Finally, tissue-resident memory T cells (T_{RM}) express numerous chemokine and adhesion receptors including CXCR3, CXCR6, CD49a and CD103, which contribute to their long-term persistence in their tissue of residence and to the surveillance of epithelial barriers exposed to microbes *(6–13)*.

Their vigorous scanning behavior makes $CD8^+$ T cells a valuable model to study amoeboid cell migration, a heterogeneous phenomenon encompassing forward and retrograde F-actin flow, as well as different types of protrusions such as lamellipodia, pseudopods and blebs *(14–19)*. Recent studies have dissected the precise mode of amoeboid migration of T_N. These cells generate a CCR7-driven retrograde cortical F-actin flow dependent on the guanine exchange factor (GEF) DOCK2 and its downstream targets Rac1 and Rac2 *(20–23)*. Retrograde F-actin flow transmits weak forces via the integrin LFA-1 to its receptor ICAM-1 displayed on stromal cells, providing the traction force for rapid T_N locomotion within the lymphoid parenchyma without inducing substantial adhesion *(23–25)*.

In addition to the paradigmatic T cell migration driven by chemosensing of external cues, we have recently uncovered a distinct motility signature displayed by submandibular salivary gland (SMG) $CD8^+$ T_{RM} *(26)*. Although these cells exhibit high *in vivo* migration speeds of 6-7 µm/min, we did not

find evidence for a substantial contribution for chemoattractant and adhesion receptors during homeostatic organ surveillance, since neither pertussis toxin treatment (to block $G_{\alpha i}$-coupled receptors) nor integrin inhibition had an effect on their motility. Instead, SMG $CD8^+$ T_{RM} spontaneously migrate with frequent shape changes in the absence of chemoattractants and specific adhesive interactions *(26)*, perhaps as an adaptation to the chemokine-poor milieu of non-inflamed salivary glands *(27)*.This is in contrast to epidermal $CD8^+$ T_{RM}, which require external chemoattractants for motility *(8, 26)*. In line with our findings, T cell lines are able to migrate in complete absence of chemokine and adhesion receptors, using topography-dependent force transmission *(28)*. Yet, the cues that trigger receptor-independent motility of $CD8^+$ T_{RM} lodging in resting glands, and the relevance of this non-canonical migration to intercept Ag-presenting cells remain unknown to date.

Here, we have systemically compared SMG T_{RM} motility to the canonical chemosensing-driven T_N amoeboid migration. In the absence of external biochemical cues, T_{RM} spontaneously generated retrograde F-actin flow as force-generating module for translocation. Furthermore, T_{RM} displayed a highly contractile actomyosin cytoskeleton, leading to continuous bleb formation at the leading edge. Autonomous cell motility was also observed in lacrimal gland T_{RM} but not T_N or small intestine T_{RM}, and was strictly dependent on their ability to sense and react to mechanical load of their microenvironment. Mechanosensing triggered an “evasion reflex”, which elicited cortical actomyosin contractility through arachidonic acid and intracellular Ca^{2+} signaling, and correlated with nuclear deformation in line with the recently uncovered function of the nucleus as mechanosensor in mammalian and non-mammalian cells *(29, 30)*. Inhibition of mechanosensing signaling disrupted T_{RM} tissue scanning and interception of target cells. In sum, our data suggest that memory T cells lodged in organs with low microbial exposure have co-opted a conserved mechanosensory module for immunosurveillance, and uncover an instructive role for physical confinement to elicit dynamic T cell motility. In combination with their preserved chemosensing capacity, our data identify a multitier strategy for T_{RM}-mediated tissue surveillance. Such a strategy bypasses the requirement for elevated constitutive chemokine and adhesion receptor expression in resting non-barrier tissues, thus preventing unwarranted leukocyte influx.

Results

SMG T_{RM} spontaneously generate retrograde F-actin flow in the absence of chemoattractants and specific adhesions

Our previous *in vivo* and *ex vivo* analysis uncovered high intrinsic SMG CD8$^+$ T_{RM} motility (**Movie 1**), which bypasses canonical chemoattractant sensing and adhesion receptor engagement *(26)*. To generate SMG CD8$^+$ T_{RM} for an in-depth examination of the underlying actomyosin cytoskeleton regulation, we adoptively transferred congenically marked OT-I TCR tg CD8$^+$ T cells, which recognize the ovalbumin (OVA) peptide $OVA_{257-264}$ in the context of H-2K^b *(31)*, into C57BL/6 mice. One day later, recipient mice were infected with lymphocytic choriomeningitis virus-OVA (LCMV-OVA), a replication-competent, attenuated LCMV variant encoding OVA as model antigen *(32)* (**Fig. 1A**). While rapidly cleared, LCMV-OVA infection results in OT-I expansion and formation of T_{CM} and T_{EM} populations in spleen and lymph nodes (LN), and *bona fide* CD103$^+$ T_{RM} in SMG at ≥ 30 d p.i. (**Fig. S1A**). Cell sizes were similar between T_N and endogenous or adoptively transferred CD8$^+$ T_{EM} and T_{RM}, while T_{CM} showed a tendency to increased cell sizes (**Fig. S1B**). Similarly, levels of the F-actin regulators phospho-Cofilin and DOCK2 were not elevated in T_{RM} as compared to other memory subsets, and expression and phosphorylation of ERM proteins, which link cortical F-actin to the plasma membrane, remained unchanged (**Fig. S1C-F**). In contrast, both endogenous and adoptively transferred SMG CD8$^+$ T_{RM} contained significantly higher F-actin levels as compared to other T cell subsets (**Fig. 1B**).

We used the F-actin probe LifeAct-GFP to examine steady-state actin cytoskeleton dynamics in T_{RM} *(33)*. We generated LifeAct-GFP$^+$ SMG OT-I T_{RM} as above and compared their cortical actin cytoskeleton dynamics to LifeAct-GFP$^+$ T_N as well-characterized benchmark, using total internal reflection fluorescence (TIRF) microscopy in an under agarose system *(23, 34–36)*. Under agarose assays allow to create promigratory conditions in the absence of a directional chemokine gradient, thus mimicking the random guided walk characteristic of T_N in lymphoid tissue and the homeostatic surveillance of T_{RM} in SMG *(23, 26, 37)*. Initially, we measured F-actin flow without cellular translocation by placing T_N and T_{RM} onto “slippery” surfaces passivated with Pluronic^{TM} F-127 (pluronic), a nonionic surfactant polyol. This approach permits to quantify cortical F-actin flow speeds occurring during spontaneous or chemokine-induced F-actin treadmilling. In the absence of

chemokines, T_N contained only sparse and short-lived cortical F-actin dots correlating with their unpolarized phenotype (**Fig. 1C and D; Movie 2**). To assess the impact of biochemical stimulation on F-actin dynamics, we added CCL19 as ligand for the T_N-expressed chemokine receptor CCR7. CCL19 rapidly induced cortical F-actin filaments that flowed from the leading to the trailing edge with speeds of 14.5 ± 8.2 µm/min (mean ± SD**; Fig. 1C and D**). This resulted in a "running on the spot"-phenotype on pluronic-passivated surfaces (**Movie 2**). When CCL19-stimulated T_N were plated on ICAM-1-coated plates, retrograde F-actin flow was converted into fast chemokinetic cell movement by force-coupling of LFA-1 to ICAM-1 as described *(23)* (**Fig. 1C and D; Movie 2**). This was accompanied by the stalling of net rearward F-actin flow, with LifeAct-GFP$^+$ F-actin becoming stationary in relation to the substrate (**Fig. 1D**).

In contrast to T_N, LifeAct-GFP$^+$ SMG T_{RM} plated on pluronic-passivated surfaces showed intrinsic cortical F-actin treadmilling from the front to the rear with speeds of 9.7 ± 6.8 µm/min (**Fig. 1C and D**), resulting in a polarized phenotype. This was accompanied by frequent F-actin protrusion formation at the leading edge (**Movie 3**). Thus, SMG T_{RM} not only contain more total F-actin but also exhibit a continuous front-to-back flow of F-actin filaments even in the absence of biochemical cues (i.e., chemokines). To assess the impact of chemokines on F-actin flow, we added CXCL10, the ligand for the T_{RM}-expressed chemokine receptor CXCR3, as these cells do not express CCR7. While the speed of retrograde cortical F-actin flow was accelerated to 12.8 ± 8.5 µm/min upon CXCL10 exposure, the increase was lower than for chemokine-stimulated T_N (**Fig. 1C and D; Movie 3**). Front-to-back F-actin flow stalled when T_{RM} were placed on lipid-free human serum albumin (HSA), which provides sufficient friction to generate traction force for cell translocation, in the absence of specific adhesive interactions (**Fig. 1C and D; Movie 3**) *(26)*. In addition, we observed occasional forward movement of F-actin filaments at the trailing edge (**Fig. 1C, dashed line**). This observation is indicative of a highly contractile uropod, which drags F-actin filaments towards the leading edge *(38)*. In sum, T_{RM} use retrograde cortical F-actin flow for translocation akin to the cortical flow-force transmission model described for motile T_N *(23, 39)*. Unlike T_N, cortical F-actin flow in T_{RM} is induced spontaneously, i.e., in the absence of external chemoattractants. Nonetheless, our data confirm that SMG T_{RM} remain responsive to CXCL10. This is in line with previous observations that CXCR3$^{-/-}$ T_{RM} do not accumulate around tissue

167 macrophage clusters *in vivo* despite scanning salivary gland parenchyma with speeds comparable
168 to wild type T_{RM} *(26)*.
169
170 *Morphometric analysis uncovers high protrusion formation in spontaneously migrating SMG T_{RM}*
171 We compared the amoeboid motility modes of T_N and T_{RM} in more detail by examining
172 displacement parameters in combination with a morphometric (i.e., cell shape) analysis. To this
173 end, we used wide-field fluorescence microscopy of T cells under agarose (without pluronic
174 passivation) and determined cell speeds, meandering index, cell area and circularity, as well as
175 numbers and sizes of leading edge protrusions using a customized analysis pipeline (**Fig. 1E and**
176 **Fig. S2**). We first compared T_N motility on HSA without CCL19 as non-migratory substrate to
177 ICAM-1 + CCL19-coated plates to mirror conditions used for F-actin flow measurements *(23)*. In
178 agreement with F-actin dynamics identified by TIRF microscopy (**Fig. 1C**), T_N converted from a
179 non-motile state with rounded cell morphology in the absence of chemokines and adhesive ligands
180 to a polarized phenotype with high speeds and directionality when ICAM-1 and CCL19 were
181 present (from 1.2 ± 0.5 µm/min to 13.1 ± 4.8 µm/min; **Fig. 1F and G; Movie 4**). T_N speeds closely
182 matched CCL19-triggered rearward F-actin flow speeds under slippery conditions (**Fig. 1G**),
183 suggesting that force coupling efficiently converts F-actin flow into forward movement. Irrespective
184 of the presence or absence of CCL19, T_N formed very few protrusions (**Fig. 1G, bottom middle**
185 **panel**).
186 In line with TIRF measurements, T_{RM} acquired a spread and polarized shape with numerous
187 protrusions and spontaneously moved on HSA-coated plates, in the absence of chemokines and
188 specific adhesive substrates (**Fig. 1F and G**). We then examined the impact of chemokine addition
189 in presence of ICAM-1 coating to recreate similar promigratory conditions as used for T_N. Whereas
190 ligands for the T_{RM}-expressed chemokine receptors CXCR3 and CXCR4 together with ICAM-1
191 augmented SMG T_{RM} speeds (from 6.7 ± 3.0 µm/min to 10.5 ± 3.1 µm/min), the increase was less
192 pronounced as in T_N (**Fig. 1G and Movie 5**). Furthermore, chemokine exposure did not increase
193 T_{RM} directionality (as assessed by the meandering index), in contrast to T_N (**Fig. 1G**). Instead,
194 chemokines reduced protrusion formation in T_{RM} (**Fig. 1G**). Taken together, autonomously moving
195 T_{RM} display a protrusion-rich amoeboid migration phenotype, which is distinct from the well-

196 characterized T_N mode *(23)*. Our data are in line with a model where protrusion formation does not
197 translate into fast leukocyte motility *(38)*, but is instead driven by retrograde F-actin flow and force
198 coupling to substrate *(23, 39)*.
199
200 *Constitutive DOCK2-Rac-Arp2/3 signaling is required for autonomous SMG T_{RM} motility*
201 Since retrograde F-actin flow can be generated by F-actin polymerization at the leading edge
202 and/or by Rho-mediated contraction of the F-actin network *(22, 40–42)*, we used under agarose
203 assays to explore the roles for Rac and Cdc42 as major drivers of Arp2/3-mediated F-actin
204 generation at the leading edge *(43)*(**Fig. S3A**). Reflecting the accumulation of the Rac GEF
205 DOCK2 at the leading edge of migrating T_{RM} (**Fig. S3B**), the DOCK2 inhibitor CPYPP *(44)* and
206 CK666, an inhibitor of the DOCK2-Rac downstream target Arp2/3 *(45)*, decreased speeds,
207 meandering index and protrusion formation in SMG T_{RM}, with a concomitant increase in circularity
208 and a decrease in cell area (**Fig. S3C and D; Movie 6**). Similarly, inhibition of Rac1 using the W56
209 peptide inhibited autonomous T_{RM} motility (**Fig. S3E and F**). In contrast, the Cdc42 inhibitor ML141
210 did not alter T_{RM} speeds and circularity, although it caused a trend to a lower meandering index
211 and a minor decrease in cellular area and average protrusion size (**Fig. S3C and D**). To
212 corroborate the roles for Rac- versus Cdc42-driven T_{RM} motility *in vivo*, we adoptively transferred
213 WT tdTom$^+$ and GFP$^+$ OT-I T cells lacking DOCK2 or the Cdc42 GEF DOCK8 into C57BL/6
214 recipients one day prior to infection with LCMV-OVA. Although DOCK2 deficiency impairs T cell
215 accumulation in non-lymphoid tissues *(46)*, we were able to identify occasional DOCK2$^{-/-}$ T_{RM} at >
216 30 days p.i. within SMG. Intravital imaging confirmed strongly reduced cell speeds and
217 directionality in the absence of DOCK2 as compared to WT T_{RM} (**Fig. S3G and H; Movie 7**).
218 DOCK8 has previously been shown to mediate T cell migration in skin *(47)*. In contrast, DOCK8$^{-/-}$
219 SMG T_{RM} moved with comparable speeds as WT T_{RM}, with only a minor reduction in directionality
220 (**Fig. S3I**). These data support a central role for leading edge DOCK2-Rac-Arp2/3-driven F-actin
221 polymerization for SMG T_{RM}-mediated tissue surveillance.
222
223 *SMG T_{RM} possess high constitutive actomyosin contractility*

We next examined the role of actomyosin contractility for spontaneous SMG T_{RM} motility. Non-muscle Myosin IIA (MYH9)-mediated contractility of F-actin filaments supports amoeboid cell motility by pulling F-actin filaments towards the trailing edge and by generating force to push the nucleus as the biggest organelle through narrow pores *(48)*. Using a reporter line expressing GFP-tagged Myosin IIA under the endogenous *Myh9* promoter *(49)*, we observed significantly higher MYH9-GFP levels in SMG OT-I T_{RM} as compared to T_{CM} and T_{EM}, suggesting a high baseline contractility (**Fig. 2A**). In under agarose assays, MYH9-GFP accumulated mostly at the trailing edge of migrating SMG T_{RM} (**Fig. 2B; Movie 8**), consistent with local F-actin contractions observed in TIRF imaging (**Fig. 1C**). MYH9-GFP also accumulated in protrusions of the leading edge, followed by their subsequent retraction (**Fig. 2B**). This observation points to a dual role for Myosin IIA activity: on the one hand, to contract the uropod, and second, to retract protrusions that are not aligned with the migratory path, as described for neutrophils *(50)*. In line with elevated MYH9 expression, SMG T_{RM} contained two to three times higher pMLC levels as compared to T_{CM} and T_{EM} (**Fig. 2C and D**).

We next attempted to genetically assess MYH9 function for SMG T_{RM} scanning, but failed to obtain MYH9-deficient peripheral T cells in a CD4-Cre x $MYH9^{fl/fl}$ line (**Fig. S4A**). Similarly, Cas9-mediated MYH9 depletion resulted in defective OT-I T cell expansion following viral infection, in line with its role in cytokinesis *(51)* (**Fig. S4B and C**). We therefore performed under agarose assays in presence of selected inhibitors of the MLC phosphorylation cascade (**Fig. 2E**). Direct inhibition of Rho using Rhosin decreased SMG T_{RM} speeds and protrusion sizes (**Fig. S5A and B**). We next evaluated its downstream effectors, myosin light chain kinase (MLCK) and Rho-associated coiled-coil kinase (ROCK), both of which regulate pMLC levels. MLCK inhibition slightly reduced T_{RM} speeds (from 7.1 ± 3.7 to 5.4 ± 3.0 µm/min; mean $\pm$ SD) but did not significantly alter directionality, cell shape and area, or protrusion formation (**Fig. 2F and G; Movie 9**). In contrast, the ROCK inhibitor Y-27632 caused cell rounding and a substantial decrease in speeds to 0.7 ± 2.7 µm/min, as well as low directionality and protrusion formation (**Fig. 2F and G; Movie 9**). Furthermore, Y-27632 blocked topography-driven T_{RM} motility on pluronic-passivated surfaces (**Fig. S5C and D**), as well as SMG T_{RM} surveillance *in situ* as assessed by intravital imaging (**Fig. S5E**). Since Rho-GTP activates nucleation factors of the formin/mDia family, we performed under

agarose assays in presence of the Formin Homology 2 domain inhibitor SMIFH2. We observed decreased T_{RM} speeds, directionality, protrusion formation and cell area in presence of this inhibitor (**Fig. S5F and G**). As caveat, SMIFH2 has been reported to affect additional factors including MYH9 *(52, 53)*. In sum, SMG T_{RM} possess high intrinsic actomyosin contractility, which is required for inherent motility and organ surveillance.

T_{RM} form blebs at the leading edge during 2D and 3D space exploration

High baseline actomyosin contractility leads to increased intracellular hydrostatic pressure that can cause bleb formation. Blebs are short-lived membrane protrusions, which form after detachment from the underlying cortical F-actin layer and can contribute to cell motility *(16)*. Blebs were recently described in sphingosine-1-phosphate-stimulated T_N *(54)* but have never been observed in resting, unmanipulated leukocytes *(55)*. We assessed whether high actomyosin contractility in SMG T_{RM} resulted in bleb formation during migration. To unequivocally distinguish F-actin-filled protrusions from blebs, we generated LifeAct-GFP x mT/mG OT-I T cells, in which F-actin and plasma membrane are tagged with GFP and tdTom, respectively (**Fig. 2H**). We transferred LifeAct-GFP x mT/mG OT-I into recipient C57BL/6 mice, followed by LCMV-OVA infection and sorting of SMG T_{RM} in the memory phase. High frame-rate *in vitro* imaging confirmed the presence of two types of leading edge protrusions: F-actin-filled protrusions and membrane blebs, which were rapidly (< 1 s) filled with F-actin (**Fig. 2I; Movie 10**). This correlated with quick accumulation of DOCK2 into blebs (**Movie 10**). We did not find evidence for formation of thin lamellipodia characteristic of lymphoblasts migrating on adhesive 2D surfaces *(56)*, perhaps owing to the low adhesiveness of HSA and the substantially lower amount of cytoplasm in resting versus activated T cells *(57)*. Both F-actin-filled protrusions and blebs were short-lived, since they were either followed by the translocation of the cell body or by retraction. Bleb formation was restricted to the leading edge of motile T_{RM} and also seen in presence of a pan-caspase inhibitor to prevent apoptotic cell death (not shown). Residual bleb formation was also observed in SMG T_{RM} treated with the DOCK2 inhibitor CPYPP (not shown). However, this did not suffice to promote cell translocation, in line with the requirement for Rac signaling to promote migration (**Fig. S3**). Finally, we also detected F-actin-filled protrusion and rapid bleb formation that bulge out into the

extracellular space at the front of T_{RM} moving in 3D collagen matrices, occasionally followed by the bulky nucleus (**Fig. 2I; Movie 10**). Bleb-supported migration is therefore suited to rapidly explore the available space in front of the cell's leading edge. Alternatively or in addition, blebs might contribute to motility and cell survival *(17, 58)*. In sum, motile T_{RM} and T_N differ in two key features: first, rearward F-actin flow in T_{RM} is generated even without external guidance cues. Second, T_{RM} possess high intrinsic actomyosin contractility correlating with formation of blebs and F-actin-filled protrusions.

Exocrine gland T_{RM} use mechanosensing to trigger polarization and motility

We next explored the cellular and molecular mechanism underlying autonomous SMG T_{RM} motility. Previous studies have shown that activated T cells migrate rapidly on 2D surfaces without confinement *(59)*. Furthermore, non-attached leukocytes can use rearward F-actin treadmilling or Myosin II-dependent membrane flow for fast translocation *(60, 61)*. To test whether this also applies to SMG T_{RM}, we examined their migration dynamics on 2D surfaces without agarose overlay, anticipating that these highly contractile cells would continue to display a polarized phenotype and motility (**Fig. 3A**). However, most T_{RM} lost their polarized cell shape and created significantly fewer protrusions on 2D surfaces as spatially confined cells did (**Fig. 3B-D**). As a result, T_{RM} displacement was essentially abolished under these conditions (**Fig. 3C and D**). Thus, T_{RM} need spatial confinement to acquire a polarized phenotype and for translocation.

To further delineate the relationship between spatial confinement, cell morphometry and autonomous motility, we exposed SMG T_{RM} to distinct mechanical loads. We adjusted the agarose concentration from 0.5% (corresponding to a Young's modulus of 2.9 kPa) to 1% (9.8 kPa) as described *(23)*. We found that T_{RM} responded to the degree of mechanical load with changes in cell shape, protrusion formation and motility parameters. When exposed to higher mechanical load (1% agarose), T_{RM} slowed down, moved less directionally, were less polarized and formed fewer protrusion. These data are consistent with a model where the forces required to lift agarose for protrusion formation and cell motility increase under high mechanical load, resulting in reduced cell migration. We then analyzed T_{RM} motility exposed to 0.125% and 0.25% agarose, assuming that reduction of the environmental resistance to deformation facilitates cell motility. Remarkably, we

found that under conditions of reduced mechanical load, T_{RM} moved more slowly, were more spherical and formed fewer and smaller protrusions as with 0.5% agarose (**Fig. 3E and F**). Thus, T_{RM} react to the degree of confinement using a mechanosensing module.

Next, we examined whether mechanosensing was a property shared with T_{RM} from other internal organs. To address this point, we isolated T_{RM} from another exocrine gland, the lacrimal gland (LG), or from the epithelial barrier of the small intestine (SI) after LCMV-OVA infection. In under agarose assays, LG but not SI T_{RM} displayed confinement-induced motility akin to SMG T_{RM} (**Fig. 3G and H**). In combination with the observation that epidermal T_{RM} do not respond to physical confinement *(26)*, these data suggest that exocrine gland but not skin or gut T_{RM} have acquired the ability to mechanosense their environment, i.e., to measure and respond to mechanical load with gradual induction of polarity and cell motility.

Confinement-induced T_{RM} motility requires nuclear mechanosensing-triggered signaling pathways

We explored the mechanism underlying cellular proprioception, which translates mechanical cell deformation into adaptive cytoskeletal dynamics. We excluded classical integrin-based mechanotransduction, since we observed T_{RM} polarization in the absence of specific integrin ligands, as well as on pluronic-passivated surfaces containing PS beads (**Fig. S5C**). The cortical actomyosin cytoskeleton itself can act as mechanosensor, but its rapid turnover (> 1 min) limits deformation sensing *(62)*. Similarly, constant vesicle trafficking at the plasma membrane renders a role for stretch-induced mechanosensing less likely *(63)*. In turn, induction of SMG T_{RM} polarity and motility by mechanical load was highly reminiscent of the “evasion reflex” shown by various mammalian and non-mammalian cell types subjected to spatial confinement. These cells use their nuclei to measure absolute environmental dimensions *(29, 30)*. According to this “nuclear ruler” model, confinement-induced mechanical unfolding of the nuclear envelope (NE) leads to activation of Ca^{2+}-dependent cytosolic phospholipase A2 (PLA2) enzymes, which act as NE stretch sensors *(63)*. The resulting production of arachidonic acid (AA) leads to membrane recruitment and activation of MYH9, which in turn stimulates sustained actomyosin contraction, bleb formation and motility *(29, 30)*, hallmarks of SMG T_{RM} migration observed here.

To examine whether SMG T_{RM} had co-opted the nucleus as mechanosensory organelle for spontaneous migration under confinement, we analyzed nuclear shape under 0.5% agarose confinement. These data confirmed that T_{RM} nuclei became stretched as reflected by increased maximal cross-section area and lower heights (**Fig. 4A and B**). To directly establish a link between mechanical cell deformation, cell morphometry and motility, we used confinement chambers with defined heights to induce nuclear compression without interfering with protrusion formation (**Fig. 4C**). At 7 µm chamber height, T_{RM} became trapped without substantial nuclear compression. Under these conditions, T_{RM} remained immotile and round, forming only sparse protrusions (**Fig. 4D**). In contrast, T_{RM} placed in 4 µm height chambers acquired a highly polarized cell shape with multiple protrusions that correlated with the induction of spontaneous motility (**Fig. 4D; Movie 11**). To examine whether mechanosensing-triggered motility can also be induced in other T cell subsets at a distinct confinement threshold, we placed SMG T_{RM} or T_N in 2-and 4 µm-high chambers. In contrast to T_{RM}, T_N did not display spontaneous motility at 4 µm confinement, while both cell populations failed to migrate under 2 µm confinement, accompanied by signs of cell death (**Fig. S6 A and B**). Thus, in the experimental conditions used here, we could not induce T_{RM}-like motility in T_N isolated from lymphoid tissue.

To further corroborate the link between nuclear deformation and confinement-induced T_{RM} motility, we used the AA analog AACOCF3 as inhibitor of PLA2 and other AA-producing enzymes (**Fig. 4E**) *(29)*. In under agarose assays, AACOCF3 treatment led to decreased T_{RM} speeds, as well as reduced directionality and number and size of leading edge protrusions (**Fig. 4F and G; Movie 12**). Addition of excess AA to AACOCF3-treated T_{RM} rescued SMG T_{RM} speeds, cell spreading, and protrusion sizes. Of note, AA-treated T_{RM} cells frequently changed direction, resulting in a low meandering index (**Fig. 4F and G; Movie 12**). These data suggest that while SMG T_{RM} are able to respond to external AA, this treatment affects the preservation of stable polarity. We examined whether other T cell populations responded similarly to AA stimulation. While addition of AA slightly increased chemokinetic T_N speeds (from 0.6 to 1.5 µm/min), this effect was much lower as compared to the impact of CCL21, suggesting that AA is not sufficient to induce robust motility in these cells. Along the same line, AACOCF3 treatment did not impair CCL21-induced T_N motility, whereas it partially reduced CXCL10-induced T_{RM} speeds and directionality (**Fig. S6C and D**).

In addition to AA production, nuclear mechanosensing requires generation of an intracellular Ca^{2+} flux, whereas extracellular Ca^{2+} is not required *(29, 30)*. To address the role for intracellular Ca^{2+} sensing, we blocked intracellular Ca^{2+} by BAPTA-AM. In parallel, we added 2APB to inhibit stretch-sensitive channels such as inositol triphosphate receptors (InsP3R), which liberate Ca^{2+} from NE and perinuclear endoplasmatic reticulum (ER) membranes. Both inhibitors resulted in a strongly decreased T_{RM} speeds, directionality, cell polarization and protrusion formation (**Fig. 4H and I; Movie 13**). Taken together, confinement-induced SMG T_{RM} migration is susceptible to inhibitors of the nuclear mechanosensing module *(29, 30)*.

Next, we analyzed whether T_{RM} expressed candidate factors involved in nuclear mechanosensing (**Fig. 4E**). The ubiquitously expressed family member cPLA2a (encoded by *Pla2g4a*) has been implied in regulating the mechanosensitive response in DCs and other cell types *(29, 30, 63)*. However, mining the Immgen database (https://www.immgen.org/) showed low to absent *Pla2g4a* expression in T cells except for double-negative thymocytes, which we confirmed by qPCR analysis (**Fig. S7A and B**). Similarly, single cell RNA sequence analysis of SMG T_{RM} failed to detect *Pla2g4a* expression (not shown). For increased sensitivity, we performed a "NanoString" multiplex gene expression analysis of factors potentially involved the mechanosensitive response by comparing sorted T_N, T_{CM}, T_{EM} and SMG T_{RM} OT-I T cells. First, we validated the sorting strategy by confirming subset-specific marker detection (**Fig. S7C**). While this sensitive approach corroborated low to absent *Pla2g4a* expression in T cells, we detected expression of *Pla2g4b*, *Pla2g10, Pla2g12a* and *Pla2g15* in T_{RM} (**Fig. S7D**). SMG T_{RM} also expressed stretch-activated InsP3Rs, which are involved in intracellular Ca^{2+} release upon nuclear compression (**Fig. S7E**) *(29, 64)*. We did not detect noticeable differences between memory T cell subset expression of factors regulating nuclear envelope structure including lamin A/C, lamin B receptor, and emerin as well as members of the Linker of Nucleoskeleton and Cytoskeleton (LINC) complex Sun1/2 and Nestrins 1-4 (**Fig. S7F and G**). Taken together, T_{RM} express several Ca^{2+} channels and PLA2 isoforms, as well as other enzymes capable of producing AA such as phospholipase B (not shown).

Mechanosensing-induced T_{RM} motility enhances target cell interception

We designed an *in vitro* system to examine the impact of T_{RM} mechanosensing on target cell encounter as a simplified tissue surveillance test. We placed SMG T_{RM} with a majority of unpulsed B cells spiked with rare cognate pMHC-pulsed, fluorescently labeled B cells in under agarose confinement (**Fig. 5A**). In this system, T_{RM} need to actively migrate to identify dispersed target cells among an excess of bystander cells. Indeed, T_{RM} were actively scanning B cells for presence of cognate pMHC (**Movie 14**). Within the observation period, almost half of the control T_{RM} (47%) were able to identify and engage with at least one target cell during the observation period, with 8% of T_{RM} interacting with four or more targets (**Fig. 5B and C**). Many interactions were short-lived and resulted in cell death as assessed by dye leakage (**Movie 14**). Addition of the PLA2 inhibitor AACOCF3 disrupted the "search and destroy" pattern (**Fig. 5B**), with only 32% and 2% of T_{RM} engaged with more than one and a maximum of four targets, respectively (**Fig. 5C**). In sum, confinement-induced random motility enhances the ability for T_{RM} to efficiently track and eliminate dispersed target cells.

In vivo interference with mechanosensing impairs SMG T_{RM} surveillance

We set out to expand our *in vitro* observations to tissue surveillance *in vivo*. Confocal analysis confirmed nuclear deformation occurring in SMG T_{RM} within dense secretory epithelium-rich tissue (**Fig. 6A**). To examine nuclear mechanosensing-triggered pathways during homeostatic SMG surveillance, we used 2PM to quantify baseline OT-I T_{RM} motility parameters in LCMV-OVA-immunized SMG before overlaying 20 or 50 μM BAPTA-AM on the SMG preparation for 20 min and recording T_{RM} motility for additional 1-4 h (**Fig. 6B; Movie 15**). BAPTA-AM has been reported to accumulate efficiently in cells *in vivo (65)*. Accordingly, the short BAPTA-AM superfusion caused a dose-dependent decrease in SMG T_{RM} speeds and directionality (**Fig. 6C-F**), with a concomitant increase in arrest coefficients and sphericity (**Fig. 6F and G**). These observations are consistent with the pronounced inhibition of T_{RM} migration by intracellular Ca^{2+} chelation in under agarose assays (**Fig. 4H and I**).

Finally, we examined whether mechanosensing contributes to SMG T_{RM} surveillance in response to a local virus rechallenge. We administered an attenuated murine cytomegalovirus (MCMV)-3D-ΔvRAP strain expressing mCherry and the $OVA_{257-264}$ peptide epitope into SMG via the Wharton's

duct of LCMV-OVA-immunized mice in the memory phase, as described *(26)*. Recipient mice were subsequently treated with DMSO or AACOCF3 for 68 h post MCMV infection (**Fig. 6H**). We chose AACOCF3 over BAPTA-AM to avoid an impact on T_{RM} function resulting from impaired intracellular Ca^{2+} flux. Intravital imaging confirmed that immediately after AACOCF3 treatment of LCMV-OVA-memory mice, the SMG T_{RM} scanning behavior was disrupted as measured by a drop in directionality, although speeds were not significantly affected in the conditions used here (**Fig. S8A and B**). This may reflect the weaker *in vitro* inhibition by AACOCF3 as compared to Ca^{2+} chelators (**Fig. 4F**). Following MCMV infection via the Wharton's duct, we administered anti-α4 and α_L (LFA-1)-blocking mAbs to prevent recruitment of circulating T cells without affecting interstitial T_{RM} motility *(26)*. Neither administration of AACOCF3 over 3 d alone or in combination with anti-α4 and LFA-1 blocking mAbs had a significant effect on total T_{RM} numbers or their CD69 and CD103 expression (**Fig. S8C and D**). In control experiments, MCMV-3D-ΔvRAP infection into one SMG lobe did not yield a significant increase in T_{RM} numbers as compared to uninfected contralateral lobes (**Fig. S8E and F**), irrespective of treatment with anti-α4 and LFA-1 integrin mAbs or the lymphocyte-sequestering drug FTY720 (**Fig. S8F and G**). These data suggested no or only limited local proliferation of SMG T_{RM} or T cell recruitment during re-challenge with the attenuated MCMV strain used here. In accordance, we observed only few $mCherry^+$ MCMV-infected cells in control- and AACOCF3-treated SMG sections at 68 h p.i. (**Fig. S8H**), in line with the key role for tissue-resident macrophages for clearance of infected cells *(26)*. Consistent with these observations, a histological analysis of MCMV-challenged SMG sections on day 3 p.i. showed comparable numbers of SMG T_{RM} in control- and AACOCF3-treated recipients (**Fig. 6J and I**). In contrast, when we examined T_{RM} distribution as a readout for inflammation-induced T cell accumulation, we observed an average of 10.5 ± 4.6 T_{RM} clusters/section (mean ± SEM; median 4.8) in control-treated SMG, with T_{RM} accumulating both in $EpCAM^{high}$ epithelial tubes and $EpCAM^{low}$ acini (**Fig. 6I and K**). In contrast, T_{RM} clustering in infected SMG was substantially reduced to 1.9 ± 1.9 clusters (median 1.3) in AACOCF3-treated recipients (**Fig. 6I and K**). Taken together, these data support a role for mechanosensing for T_{RM} tissue surveillance of exocrine glands as a complementary mechanism to canonical motility driven by biochemical cues (**Fig. 6L**) *(29, 30, 66, 67)*.

Discussion

$CD8^+$ T_{RM} surveille organs with diverse tissue architecture, cellular and extracellular matrix composition and degrees of microbial exposure. Conceivably, organ surveillance is accomplished by local adaptations of their patrolling modus to enable efficient cell scanning and interception of re-emerging viral infections. In epithelial barriers that are constitutively exposed to microbes, chemokines and integrin ligands contribute to T_{RM} surveillance *(6–12)*. Here, we report that exocrine gland T_{RM} possess the capacity of spontaneous F-actin treadmilling, which endows them with an internal force generation module that bypasses the requirement for chemoattractant and adhesion receptor sensing. Instead, a mechanosensing module assists these cells to measure the degree of confinement-induced mechanical load. This module is coupled to a promigratory response and is susceptible to inhibitors of the nuclear mechano-gauge, implying a non-genetic function of the nucleus in this process. Thus, in these non-barrier organs with low constitutive chemokine expression *(27)*, memory T cell subsets are equipped to sense and react to the physical properties of their tissue of residence, extracting promigratory cues from spatial confinement for baseline surveillance. At the same time, they retain their chemosensing capacity to complement their protective function during infection, suggesting a multitiered surveillance strategy.

Amoeboid cell migration is based on continuous polymerization of F-actin at the leading edge and contraction of F-actin filaments by myosin motors at the trailing edge of the cell *(48)*. Both processes contribute to the generation of a net retrograde F-actin flow, which amoeboid cells exploit to generate forward locomotion via mechanical coupling to a substrate or liquid. Depending on the cell type examined, amoeboid migration spans a continuum from mostly Rho-driven actomyosin contractility-driven (as in some DCs) to mostly Rac-driven motility lacking protrusions (as in T_N) *(23, 42)*. Our data suggest that SMG T_{RM} acquire a blend of these migration modes, presumably as an adaptation to the confined microenvironment of exocrine glands *(26)*. Despite these adjustments, a DOCK2-Rac-Arp2/3 signaling axis is preserved in T_N and T_{RM}, suggesting a similar molecular wiring of their basic force-generating module in both cell subsets. While chemokine receptors create mechanical force by activating the DOCK2-Rac-Arp2/3 module in T_N, it is currently not known how DOCK2-driven F-actin treadmilling is regulated in T_{RM}. Conceivably, a

global increase in expression of proteins associated with small GTPase signaling or a decreased expression of negative regulators of this pathway might facilitate spontaneous F-actin formation. As example, F-actin filament density grows with the square of actin nucleation-promoting factor membrane density *(68)*. At the same time, T_{RM} are characterized by increased expression of RGS1 and RGS2, negative regulators of chemoattractant receptor signaling *(69)*. This may explain the limited impact of chemokine addition to T_{RM} locomotion as compared to T_N. Nonetheless, the residual capacity of T_{RM} to respond to chemoattractants suffices for their accumulation at spots of viral reemergence *(8, 26)*.

Our data further expose that mechanical load suffices to trigger exocrine gland T_{RM} polarization and motility, accompanied by increased cortical actomyosin contractility. Mechanosensing is increasingly acknowledged to play a central role in the immune system *(70–73)*. On a molecular level, T cells use their TCR as mechanosensitive receptor to gauge pMHC affinity and for target cell elimination, in a process called mechanosurveillance *(74, 75)*. In the innate immune system, mechanical cues detected by Piezo1 ion channels in macrophages contribute to lung inflammation *(76)*, and subsets of spleen DCs use adhesion GPCR as cues for proper positioning close to venous sinusoids *(77)*. The influence of physical properties on leukocyte migration in complex environments is also well documented *(5, 16, 17, 19, 70, 78, 79)*. In most cases, physical constraints are typically considered barriers to leukocyte dissemination, as is the case for basement membranes separating endothelial and epithelial cell layers from the interstitium *(80)*. In contrast, we show here that exocrine gland T_{RM} respond to intermediate levels of confinement-induced mechanical load with vigorous motility that required high Myosin IIA-driven contractility. Thus, while confinement is often associated with impaired motility, exocrine gland T_{RM} exploit local tissue properties to transform mechanical shape deformations into cytoskeletal rearrangements. Our data further show that T_{RM} mechanosensing is susceptible to pharmacological inhibitors of signaling pathways induced by nuclear compression. Until recently, the nucleus has been mainly considered as a passive storage for genetic information. Furthermore, as the cell's biggest organelle, the nucleus constitutes a major obstacle to cellular passage through constricted spaces *(81)*. Yet, recent findings in DC and other leukocytes have uncovered a central role for the nucleus in selecting the migratory path by determining permissive pore sizes *(82)*. In keeping with this, the

nucleus also serves as central element for cellular proprioception. Much like humans sense their environment through sight, hearing, touch and smell to react adequately, recent studies have provided compelling evidence for nuclear deformation and an autonomous contractile response as the cellular correlate of a sense of space and pressure *(66, 83)*. To accomplish this feat, the nucleus measures absolute dimensions through the stretching of its NE, which beyond a cell-specific setpoint triggers an "evasive reflex" via increased cortical contractility and spontaneous cell translocation *(29, 30)*. Given its low constitutive membrane trafficking, the quiescent NE is particularly suited as low noise detector to convert mechanical perturbations into chemical signals as compared to plasma membranes, which display rapid turnover *(84)*. To date, the precise factors generating AA and other signals involved in nuclear mechanosensing are not well characterized owing to the complex cell-type-specific regulation of lipid metabolism and Ca^{2+} channel expression *(85–87)*. As example, the cPLA2a isoform, which has been implicated in regulating the contractile response in DCs and zebrafish progenitor stem cells *(29, 30, 88)*, is absent or only expressed at very low levels in mature T cells. Together with the fact that compensatory mechanisms between different isoforms might occur, genetic approaches to disrupt mechanosensing in T_{RM} constitute a formidable challenge. Despite these caveats, the combined data describing i) the close correlation of mechanical load, nuclear deformation and induction of polarization and motility, and ii) the impact of pharmacological inhibitors of the nucleosensing module AACOCF3, BAPTA-AM and 2APB on cell shape and motility, are coherent with the published nuclear ruler-based mechanosensing model *(29, 30)*.

While many cell types display a Ca^{2+} and PLA2-mediated response upon nuclear disturbance *(29, 30, 63)*, our data suggest that mechanosensing-driven motility is not a universal feature of all T cell subsets, at least not in the experimental conditions applied here. Thus, T_N, T_{CM} and T_{RM} lodged in gut and skin epithelium do not spontaneously move when placed under confinement *(26)*. For the latter population, this may reflect their greater dependence on $G\alpha_i$-coupled signaling as compared to exocrine T_{RM} *(8)*. Local chemokines induced by constant microbial exposure might help to avoid accidental egress of epithelial T_{RM} outside the host by restricting them in close vicinity to the basement membrane. In turn, mechanosensing-triggered motility for baseline surveillance might be preferentially induced in tissues with limited microbial exposure, where steady-state chemokine

levels are low *(27)*. This surveillance strategy equips T_{RM} with flexibility to surveille multiple organs with diverse cellular and matrix composition, while retaining responsiveness to inflammation-triggered local chemokine gradients.

As a limitation, despite providing solid evidence for mechanosensing capacities in T_{RM} subsets, the molecular pathways involved in this process remain undefined. Furthermore, the use of pharmacological inhibitors to interfere with confinement-induced T_{RM} motility might affect additional signaling pathways in these cells, or influence bystander cells in *in vivo* experiments. Along the same line, the *in vivo* pharmacokinetics of the PLA2 and Ca^{2+} flux inhibitors are not well defined, rendering an assessment of the degree of inhibition after administration difficult. Finally, our study does not address to which extent mechanosensing is a property shared with other leukocytes, such as NK cells lodged in exocrine glands.

In sum, while is well-established that the transition of T_N to T_{EFF} and memory T cell subsets is accompanied by changes in the chemoattractant and adhesion receptor repertoire, our data suggest that these changes do not fully explain the scanning behavior of these cells in distinct organs. Thus, physical properties of the tissue of residency are integrated by adaptive immune cells with local biochemical cues for a specific multitier immune surveillance strategy. It is conceivable that mechanosensing elicits site-specific signaling, epigenetic and metabolic adaptations in local immune cell populations, encouraging further investigation into the underlying molecular regulation.

Materials and Methods

Study design

The aim of this study was to examine the mechanisms underlying intrinsic motility of SMG T_{RM}. To this end, we systemically administered LCMV-OVA and isolated Ag-specific $CD8^+$ T cells from SMG and other organs. We applied *ex vivo* migration assays, immunofluorescence, intravital imaging, gene expression analysis and flow cytometry to compare their migration requirements with $CD8^+$ T_N. Furthermore, we administered pharmacological inhibitors of small GTPase and nuclear mechanosensing signaling pathways to functional assays. Last, we assessed the role of the T_{RM} mechanosensing module for target finding and cell clustering after viral re-challenge. Mice or isolated T cells were randomly assigned to experimental groups and analyzed without excluding outliers, and experimenters were not blinded. The number of independent experiments is indicated in the figure legend.

Mice

Tg(TcraTcrb)1100Mjb ("OT-I") TCR transgenic mice *(31)* were backcrossed to C57BL/6-Tg(CAG-EGFP)1Osb/J ("GFP^+") *(89)*, hCD2-dsRed ("$dsRed^+$") *(90)*, tdTomato-expressing Ai14 x ZP3 ("$tdTom^+$") *(91, 92)*, mT/mG *(93)* and LifeAct-GFP lines *(33)*. GFP^+ OT-I were further crossed to CD4-Cre x $MYH9^{flox/flox}$ *(94)*, $DOCK2^{-/-}$ *(40)* and $DOCK8^{-/-}$ *(95)* lines and $dsRed^+$ OT-I to the MYH9-GFP reporter line *(49)*. DOCK2-GFP were described before *(96)*. All mice were bred at the animal facility of the University of Fribourg, Switzerland, and were used as lymphocyte donor mice. Six-to-ten weeks-old male and female sex-matched C57BL/6JRj mice (Janvier, Le Genest-Saint-Isle, France) were used as recipient mice. All experiments were performed in accordance to federal animal experimentation regulations and approved by the cantonal committee (FR_2021_24, FR_2021_25, FR_2021_30).

T cell transfer and viral infections

$CD8^+$ T cells were negatively isolated from spleen and peripheral LNs using the EasySep™ Mouse $CD8^+$ T cell Isolation Kit (Stem Cell Technologies) or the MojoSort Mouse $CD8^+$ T cell Isolation Kit

588 (BioLegend) according to manufacturer's instructions. OT-I T cells (5 x 10^4) were i.v. transferred
589 into recipient mice 24 h before i.p. infection with 10^5 pfu LCMV-OVA *(32)*.
590
591 *Reagents*
592 Sodium pyruvate (P04-43100), HEPES buffer (P05-01100), minimum essential medium non-
593 essential amino acids (MEM NEAA, P08-32100), L-glutamine 200mM (P04-80100) and PenStrep
594 (P06-07100) were purchased from PAN Biotech and RPMI 1640 (#21875-034) and Fetal Bovine
595 Serum (FBS, 10270-106) were from Gibco. CPYPP (Tocris) was used at 50 µM, CK666 (R&D) at
596 100 µM, ML141 (Tocris) and MLCK inhibitor peptide 18 (Calbiochem) at 20 µM, Y27632 (Sigma-
597 Aldrich or Hello Bio) at 20 µM or 200 µg/mouse *in vivo*, AACOCF3 (Tocris or Enzo Life Sciences)
598 at 20 µM or 300 µg/mouse *in vivo*, BAPTA-AM (Cayman Chemical) at 10 µM, arachidonic acid
599 (Cayman Chemical) at 70 µM, 2APB (Tocris) at 100 µM, W56/F56 (R&D) at 100 µM and Rhosin
600 (Sigma-Aldrich) at 10 µM.
601
602 *Flow cytometry analysis*
603 At indicated time points, spleens and LNs were harvested and organs were passed through cell
604 strainers (70 µm; Bioswisstec) to obtain single-cell suspensions. Red blood cell lysis was
605 performed on splenocytes. SMG were minced and treated with 2 kU/ml collagenase II (Gibco) and
606 1 kU/ml DNase I (Roche) in CMR RPMI1640/10% FCS/0.1 mM non-essential amino acids/10 mM
607 HEPES/100 U/ml penicillin/0.1 mg/ml streptomycin/2 mM L-glutamine/1 mM sodium pyruvate) for
608 30 min at 37°C, passed through a 70-µm cell strainer, and washed with PBS/5 mM EDTA. Cell
609 suspensions were stained with Zombie Fixable Viability Kit (BioLegend) for 15 min on ice. Fc
610 receptors were blocked with an anti-mouse CD16/32 antibody (BioLegend) for 10 min on ice. Cell
611 surface staining was performed in FACS buffer (PBS/2% FCS/1 mM EDTA) for 20 min on ice using
612 the following antibodies:

Antibody	Clone	Company	Order number
Anti-CD8α-APC/Fire750	53-6.7	BioLegend	100766
Anti-CD44-BV605	IM7	BioLegend	103047
Anti-CD45-BV711	30-F11	BioLegend	103147
Anti-CD62L-BV421	MEL-14	BioLegend	104436
Anti-CD103-APC	2E7	BioLegend	121414

Cell suspensions were washed with FACS buffer (PBS/2% FCS/1 mM EDTA) and fixed and permeabilized using the BD Cytofix/Cytoperm kit following the manufacturer's instructions. Intracellular staining was performed for 40 min on ice using the following antibodies or Phalloidin-TRITC (Sigma-Aldrich) in Perm-Wash solution:

Antibody	Clone	Company	Order number
Anti-ERM	polyclonal	Cell Signaling	3142
Anti-pCofilin	polyclonal	Cell Signaling	3313
Anti-pERM	polyclonal	Cell Signaling	3141
Anti-pMLC	polyclonal	Cell Signaling	3674

Cell suspensions were washed with Perm/Wash and stained with Biotin-SP AffiniPure Goat Anti-Rabbit IgG (Jackson Immuno Research, 111-065-144) for 40 min on ice before washing again and staining with streptavidin-PE (BioLegend) for 20 min on ice. Cells were washed again and acquired on Attune NxT Flow Cytometer (ThermoFisher) or LSR Fortessa (BD). Data were analyzed with FlowJo.

Immunofluorescence

OT-I memory cells were isolated from SMG and spleen at > 30 d p.i. LCMV-OVA-infected C57BL/6 mice. Single cell suspensions of SMG and spleen were generated as above and sorted for tdT^+ T cells. Ibidi sticky slides (untreated side) with a 12-well removable chamber were coated with 10 μg/ml fibronectin (Sigma-Aldrich). Cells were added and incubated 2 h at 37°C, fixed with 4% paraformaldehyde for 20 min at RT, washed and permeabilized using BD Fixation/Permeabilization solution 20 min at 4°C. Cells were blocked with BD Perm/Wash 2% goat serum for 1 h at RT, stained with rabbit anti-pMLC (Cell signaling, 3674) o.n. at 4°C, washed, stained with a goat anti-rabbit AF647 (Invitrogen, A32733) for 1 h at RT and washed again. The 12-well removable chamber was removed and the sticky slide was mounted on a glass slide with Prolong Gold Antifade with DAPI (ThermoFisher) and let dry at RT for 24 h. Images were taken with a Leica SP5 confocal microscope using a 63x glycerin objective (APO CS, NA 1.3). Data were analyzed with Imaris (Bitplane). For SMG sections, SMG were frozen in OCT and cryosectioned for

638 immunofluorescence (6 or 10 µm), followed by labeling with goat anti-GFP (Rockland, 600-101-
639 215) and anti-EpCAM AF647 (BioLegend, 118212) for epithelium,
640
641 *2PM image acquisition and analysis*
642 2PM intravital imaging of SMG was performed as described *(97)*. In brief, mice were anesthetized
643 with ketamine/xylazine/acepromazine and the right SMG lobe was surgically exposed. Baseline
644 image sequences were acquired before 200 µg/mouse Y27632 or 300 µg/mouse AACOCF3 were
645 injected i.p. Alternatively, BAPTA-AM (20 or 50 µM) was overlaid in saline for 20 min. Twenty min
646 to 3 h after Y27632 or 1 to 4 h after AACOCF3 or BAPTA-AM administration, further image
647 sequences were recorded of the same surgical preparation. 2PM imaging was carried out with a
648 TrimScope 2PM system (LaVision Biotec) using a 25X Nikon (NA 1.0) objective and a Ti:sapphire
649 laser (Mai Tai HP, Spectraphysics) tuned to 780 or 840 nm. ImSpector software was used to
650 control the 2PM system and acquire images with an automated system providing real-time drift
651 correction *(98)*. Eleven to sixteen x-y slices with a z-step size of 4 µm were acquired in 0-100 µm
652 depth with a time interval of 20 s for 20-30 min. Emitted light and second harmonic signals were
653 detected through 447/55-nm, 525/50-nm, 593/40-nm and 655/40-nm bandpass filters with non-
654 descanned detectors. Data were analyzed with Imaris (Bitplane) and a customized script for arrest
655 coefficient analysis with a threshold of 4 µm/min as described *(26)*.
656
657 *Under agarose and confinement chamber assays*
658 T_N were isolated from spleen and PLN of a naive mouse using the EasySep™ Mouse $CD8^+$ T cell
659 Isolation Kit (Stem Cell Technologies) or the MojoSort Mouse $CD8^+$ T cell Isolation Kit (BioLegend)
660 according to manufacturer's instructions. T_{RM} were isolated from SMG, LG or SI of > 30 d LCMV-
661 OVA-infected C57BL/6 mice by flow cytometry sorting. A 17-mm diameter circle was cut into the
662 center of 60-mm dishes. The hole was sealed from the bottom part of the dish using aquarium
663 silicone (Marina) and a 24-mm glass coverslip or an Ibidi sticky slide. After the silicone dried, we
664 overlaid a 5 mm-high ring cut from a 15-ml falcon tube and sealed the borders with aquarium
665 silicone. For T_{RM} migration coverslips were washed with PBS and coated with 2% fatty acid-free
666 human serum albumin (HSA; A-1887, Sigma) for 1 h at 37°C. For a “slippery” surface, Ibidi sticky

slides (untreated side) were coated with 1% Pluronic F-127 (Invitrogen, P6866) for 1 h at RT. For T_N migration coverslips were coated with 20 µg/ml Protein A (6500-10, BioVision) for 1 h at 37°C, washed 3 times with PBS and blocked with 1.5 % BSA for 1 h at 37°C. After washing once with PBS, cover glasses were coated for 2 h at 37°C with 100 nM recombinant ICAM1-Fc (796IC, R&D Systems) and washed 2 times with PBS. The coverslips were blocked again with 1.5 % BSA for 1 h at 37°C and washed once with PBS. Five ml of 2 x HBSS and 10 ml of 2 x CMR containing 1% HSA (for T_{RM}) and 20% FBS (for T_N) were mixed and heated in a water bath to 56°C. One hundred mg SeaKem Gold Agarose (50152, Lonza) was dissolved and heated in 5 ml MilliQ water before adding to the prewarmed medium to give a final 0.5% agarose concentration. After cooling down to 37°C, 500 µl of the agarose mix was added on top of the coverslip. For T_N experiments, 100 nM CCL19 (Peprotech, 250-27B) were added to the agar. The agar was let to solidify first 5 min at RT and then 20 min at 4°C. We punched a sink hole (diameter approximately 2 mm) in the agarose on the side. For experiments with inhibitors, cells were incubated with the inhibitor for 1 h at 37°C before the experiment and the inhibitor was also present in the agarose. Sorted or isolated T cell populations were pelleted in an Eppendorf tube. In some experiments, 2 x 10^4 SMG T_{RM} were mixed with 0.2 x 10^6 1 nM $OVA_{257-264}$-pulsed B cells isolated using the EasySep™ Mouse B cell Isolation Kit (Stem Cell Technologies) and labelled with 2.5 µM CMTMR together with 1 x 10^6 unpulsed, non-labelled B cells in the presence of 100 ng/ml BAFF (R&D systems, 8876-BF-010). Cells were resuspended in the smallest possible achievable volume (ca. 2-5 µl) and 1 µl were injected in the opposite side from the sink hole using a 2.5-µl Eppendorf pipette. From the sink hole, surplus of medium was collected to confine cells between the agarose and the glass slide. Time-lapse images were taken from the center of the dish using a Zeiss fluorescent microscope (AxioObserver, Zeiss) or a GE DeltaVision Elite widefield fluorescent microscope (U plan, S Apo, NA 0.75). Images were taken every 20 s for 15-20 min. For the TIRF images the GE DeltaVision microscope was used with a laser module and a 60X TIRF objective.

A Dynamic Cell Confiner device (4Dcell, France) was used to study T_{RM} cell migration under defined chamber heights. Polydimethylsiloxane suction cups with 4 µm or 7 µm-high micropillars were prepared as described in the manufacturer's instructions. Plates were coated with 2% HSA. Sorted SMG T_{RM} (10^5 cells) were transferred into each plate. Before imaging, the suction cup was

plugged to an adjustable vacuum source. Once confined at a pressure from -50 to -100 mbar, cells were imaged with a GE DeltaVision microscope as above.

Dynamic and morphometric cell analysis

Cortical F-actin flow in TIRF image sequences was measured using the Imaris (Bitplane) particle tracking function to generate tracks of GFP^+ F-actin speckles, as previously described *(35, 36, 99)*. The global speed depicts displacement over tracking time for each track. Morphometric data were analyzed with Imaris or a custom-made FIJI plugin (source code is available at https://github.com/MatthieuPalayret/DynMorpho_Analysis). For dynamic and morphometric cell analysis, cell contours were determined using the ADAPT plugin *(100)*. Cells which areas were exceedingly high or low (<505 $pixel^2$ and >10,000 $pixel^2$) were excluded. Intersecting cell contours in consecutive frames were linked to form cell trajectories. When a trajectory evidenced a dramatic increase or decrease of the area of its cell in consecutive frames (with a ratio of areas > 150%), this was interpreted as the encounter or the separation of two distinct trajectories, and the original trajectory was consequently split in two (one trajectory ending before this event, and the other one beginning after it). Trajectories shorter than 6 frames were discarded. All trajectories were further visually qualitatively confronted to the original acquisition, and incorrect trajectories were manually split or rejected. For each cell contour in each frame, protrusions were defined as regions of the cells where the curvature (averaged over a specified window of 6 pixels of radius) of its contour was negative, denoting a zone with concave extrema (**Fig. S2**). When the area of a protrusion was smaller than a specified value (30 $pixel^2$) or larger than a specified proportion of the area of the cell (> 30%), the protrusion was excluded from further analysis. Finally, to exclude the uropod from the protrusion analysis, a uropod was defined as the furthest protrusion from the leading edge of the cell (as defined by the direction taken by the cell from its positions in the previous two frames).
For each trajectory, the dynamic and morphometric analysis consisted in calculating six outputs: the average speed of the cell; the meandering index of the trajectory, which is a measure of its linearity, calculated as the ratio of the distance separating the initial and final points of the trajectory over the distance travelled by the cell (the ratio equals 1 if the trajectory is exactly linear); the average area of the cell; its average circularity coefficient, calculated as the average over the

trajectory, of the ratio of the true area of the cell over the area of a circular cell which would have the same perimeter (= 4π x area/perimeter^2 - the coefficient equals 100 when the cell is perfectly circular); and both the average number and size of the protrusions of the cell (the uropod being excluded) over its whole trajectory.

3D collagen matrix migration

T_{RM} migration through a confined three-dimensional collagen type I matrix was performed in µ–Slide Chemotaxis ibiTreat chambers (ibidi, Switzerland) as described *(101)*. Briefly, sorted LifeAct-GFP x mT/mG T_{RM} were resuspended at 5 x 10^5 cells/ml in RPMI 1640 medium supplemented with 10% heat inactivated FCS. 30 µl PureCol collagen I (CellSystems, Troisdorf, Germany), 4 µl 10x DMEM, and 2 µl 7.5% $NaHCO_3$ were premixed, carefully mixed with 18 µl cell suspension, and applied to µ-slide chemotaxis chambers. Collagen was allowed to polymerize for 40 min at 37°C in a humidified incubator. Live cell imaging was performed on a laser scanning microscope (Leica TCS SP5; Leica, Switzerland) using an HCX PL APO CS 63.0x (NA1.40) OIL UV objective at 0.65 sec intervals on a microscope stage fitted with a Tokai Hit Thermoplate at 37°C.

MCMV rechallenge and cluster analysis

MCMV rechallenge experiments were performed as described *(26)*. In brief, GFP^+ OT-I cells (5 x 10^4/mouse) were transferred into C57BL/6 mice and i.p. infected on the following day with 10^5 pfu LCMV-OVA. At > 30 d p.i., mice were treated with vehicle (DMSO) or 300 µg $AACOCF_3$, together with anti-α4 (clone PS/2) and anti-α_L (LFA-1) (clone FD441.8; each 100 µg/mouse) mAbs *(26)*. After 2 h, 10^6 pfu of the attenuated MCMV-3D-ΔvRAP strain expressing the SIIINFEKL peptide epitope *(102)* were locally administered to the right SMG via Wharton's duct injection. Recipient mice were treated every 12 h with 300 µg AACOCF3 or vehicle (final volume 100 µl in saline) and at 48 h p.i. again with PS/2 and FD441.8 as above. Alternatively, we administered daily 2 µg/g body weight FTY720. On day 3 (68 h after MCMV injection), mice were perfused with 4% PFA and the right SMG was harvested, fixed o.n. at 4°C in 5 mL 4% PFA/PBS, transferred into 30% sucrose and kept at 4°C for 24 h. SMG were frozen in OCT and cryosectioned for immunofluorescence (6 or 10 µm), followed by labeling with goat anti-GFP (Rockland, 600-101-215) and donkey anti-goat

AF488 (ThermoFisher, A11055), and rabbit anti-RFP (Abcam, ab62341) and donkey anti-rabbit AF555 (ThermoFisher, A32794), for viral foci. Tile scans were obtained by widefield (DeltaVision) or confocal (Leica Stellaris Falcon 8) fluorescence microscopy and T_{RM} were identified using the Imaris "spots" function. 9 neighbor-clusters were empirically defined by choosing a maximum distance of 62 µm between spots. The percentage of clustered cells was obtained by dividing the number of clustered over total number of spots.

Statistical analysis

Two-tailed, unpaired Student's t-test, Mann-Whitney U-test, one-way ANOVA with Dunn's multiple comparisons test, Kruskal-Wallis test, or a Wilcoxon rang test was used to determine statistical significance (Prism, GraphPad). Whiskers in "box and whisker" plots depict a range of 90-100% of individual values (non-included values are shown as individual dots), while the box comprises 50% of all data points and the line within the box displaying the median. Significance was set at $p < 0.05$.

Supplementary materials

Figure S1. Flow cytometry of memory T cells.

Figure S2. Outline of morphometric analysis.

Figure S3. Autonomous SMG T_{RM} motility requires constitutive DOCK2-Rac-Arp2/3 signaling.

Figure S4. Genetic depletion of MYH9 impairs T cell development and *in vivo* expansion.

Figure S5. SMG T_{RM} motility requires Rho signaling.

Figure S6. T cell motility under confinement.

Figure S7. Gene expression analysis.

Figure S8. Characterization of SMG viral rechallenge experiment and inhibitors.

Movie 1. Intravital imaging of OT-I T_{RM} migration in SMG during the memory phase following LCMV-OVA infection.

Movie 2. TIRF time-lapse video of F-actin dynamics in LifeAct-GFP$^+$ OT-I T_N in under agarose assay.

782 Movie 3. TIRF time-lapse video of F-actin dynamics in LifeAct-GFP^{+} SMG OT-I T_{RM} in under
783 agarose assay.
784 Movie 4. Widefield fluorescent microscopy time-lapse video of OT-I T_{N} in under agarose assay on
785 HSA or CCL19 and ICAM-1.
786 Movie 5. Widefield fluorescent microscopy time-lapse video of SMG OT-I T_{RM} in under agarose
787 assay on HSA or CXCL10, CXCL10 and ICAM-1.
788 Movie 6. Widefield fluorescent microscopy time-lapse video of SMG OT-I T_{RM} in under agarose
789 assay on HSA and CPYPP or CK666.
790 Movie 7. Intravital imaging of DOCK2$^{-/-}$ and WT OT-I T_{RM} in SMG during the memory phase
791 following LCMV-OVA infection.
792 Movie 8. Widefield fluorescent microscopy time-lapse video of DsRed^{+} MYH-GFP^{+} SMG OT-I T_{RM}
793 in under agarose assay on HSA.
794 Movie 9. Widefield fluorescent microscopy time-lapse video of SMG OT-I T_{RM} in under agarose
795 assay on HSA and MLCK or Y-27632.
796 Movie 10. Widefield fluorescent microscopy time-lapse video of mT/mG^{+} LifeAct-GFP^{+} or DOCK2-
797 GFP^{+} SMG OT-I T_{RM} in under agarose assay, followed by confocal microscopy time-lapse image
798 sequence of mT/mG^{+} LifeAct-GFP^{+} SMG OT-I T_{RM} in 3D collagen matrix.
799 Movie 11. Widefield fluorescent microscopy time-lapse video of SMG OT-I T_{RM} in confinement
800 chamber with micropillars of 7 μm or 4 μm height.
801 Movie 12. Widefield fluorescent microscopy time-lapse video of SMG OT-I T_{RM} in under agarose
802 assay on HSA with EtOH, $AACOCF_3$ and $AACOCF_3$ + AA.
803 Movie 13. Widefield fluorescent microscopy time-lapse video of SMG OT-I T_{RM} in under agarose
804 assay on HSA with DMSO, BAPTA-AM and 2APB.
805 Movie 14. Widefield fluorescent microscopy time-lapse video of SMG OT-I T_{RM} in under agarose
806 assay on HSA with $OVA_{257-264}$-pulsed and unpulsed B cells with or without $AACOCF_3$.
807 Movie 15. Intravital imaging of SMG T_{RM} before and after BAPTA-AM (50 μM) superfusion.
808

References

1. J. W. Griffith, C. L. Sokol, A. D. Luster, Chemokines and Chemokine Receptors: Positioning Cells for Host Defense and Immunity. *Immunology* 32, 659–702 (2014).

2. J. V. Stein, N. Ruef, Regulation of global CD8+ T-cell positioning by the actomyosin cytoskeleton. *Immunol Rev* 289, 232–249 (2019).

3. D. Masopust, J. M. Schenkel, The integration of T cell migration, differentiation and function. *Nat Rev Immunol* 13, 309–320 (2013).

4. J. R. Groom, Regulators of T-cell fate: Integration of cell migration, differentiation and function. *Immunol Rev* 289, 101–114 (2019).

5. D. J. Fowell, M. Kim, The spatio-temporal control of effector T cell migration. *Nat Rev Immunol* 21, 582–596 (2021).

6. N. Iijima, A. Iwasaki, Tissue instruction for migration and retention of TRM cells. *Trends Immunol* 36, 556–564 (2015).

7. S. N. Mueller, L. K. Mackay, Tissue-resident memory T cells: local specialists in immune defence. *Nat. Rev. Immunol.* 16, 79–89 (2016).

8. A. Zaid, J. L. Hor, S. N. Christo, J. R. Groom, W. R. Heath, L. K. Mackay, S. N. Mueller, Chemokine Receptor–Dependent Control of Skin Tissue–Resident Memory T Cell Formation. *J. Immunol.* 199, 2451–2459 (2017).

9. P. C. Rosato, L. K. Beura, D. Masopust, Tissue resident memory T cells and viral immunity. *Curr Opin Virol* 22, 44–50 (2017).

10. P. A. Szabo, M. Miron, D. L. Farber, Location, location, location: Tissue resident memory T cells in mice and humans. *Sci Immunol* 4, eaas9673 (2019).

11. S. C. Sasson, C. L. Gordon, S. N. Christo, P. Klenerman, L. K. Mackay, Local heroes or villains: tissue-resident memory T cells in human health and disease. *Cell. Mol. Immunol.* 17, 113–122 (2020).

12. S. K. Bromley, H. Akbaba, V. Mani, R. Mora-Buch, A. Y. Chasse, A. Sama, A. D. Luster, CD49a Regulates Cutaneous Resident Memory CD8+ T Cell Persistence and Response. *Cell Reports* 32, 108085 (2020).

13. M. Heeg, A. W. Goldrath, Insights into phenotypic and functional CD8+ TRM heterogeneity. *Immunol. Rev.* (2023), doi:10.1111/imr.13218.

14. P. Friedl, B. Weigelin, Interstitial leukocyte migration and immune function. *Nat Immunol* 9, 960–969 (2008).

15. T. Lämmermann, M. Sixt, Mechanical modes of ‘amoeboid’ cell migration. *Curr Opin Cell Biol* 21, 636–644 (2009).

16. D. L. Bodor, W. Pönisch, R. G. Endres, E. K. Paluch, Of Cell Shapes and Motion: The Physical Basis of Animal Cell Migration. *Dev Cell* 52, 550–562 (2020).

17. E. K. Paluch, I. M. Aspalter, M. Sixt, Focal Adhesion-Independent Cell Migration. *Annu Rev Cell Dev Biol* 32, 469–490 (2016).

18. L. K. Fritz-Laylin, The evolution of animal cell motility. *Curr Biol* 30, R477–R482 (2020).

19. S. SenGupta, C. A. Parent, J. E. Bear, The principles of directed cell migration. *Nat Rev Mol Cell Bio* 22, 529–547 (2021).

20. T. Okada, J. G. Cyster, CC Chemokine Receptor 7 Contributes to Gi-Dependent T Cell Motility in the Lymph Node. *J Immunol* 178, 2973–2978 (2007).

21. T. Worbs, T. R. Mempel, J. Bölter, U. H. von Andrian, R. Förster, CCR7 ligands stimulate the intranodal motility of T lymphocytes in vivo. *J. Exp. Med.* 204, 489–495 (2007).

22. M. Faroudi, M. Hons, A. Zachacz, C. Dumont, R. Lyck, J. V. Stein, V. L. J. Tybulewicz, Critical roles for Rac GTPases in T-cell migration to and within lymph nodes. *Blood* 116, 5536–5547 (2010).

23. M. Hons, A. Kopf, R. Hauschild, A. Leithner, F. Gaertner, J. Abe, J. Renkawitz, J. V. Stein, M. Sixt, Chemokines and integrins independently tune actin flow and substrate friction during intranodal migration of T cells. *Nat. Immunol.* 19, 606–616 (2018).

24. E. Woolf, I. Grigorova, A. Sagiv, V. Grabovsky, S. W. Feigelson, Z. Shulman, T. Hartmann, M. Sixt, J. G. Cyster, R. Alon, Lymph node chemokines promote sustained T lymphocyte motility without triggering stable integrin adhesiveness in the absence of shear forces. *Nat Immunol* 8, 1076–1085 (2007).

25. R. T. Boscacci, F. Pfeiffer, K. Gollmer, A. I. C. Sevilla, A. M. Martin, S. F. Soriano, D. Natale, S. Henrickson, U. H. von Andrian, Y. Fukui, M. Mellado, U. Deutsch, B. Engelhardt, J. V. Stein, Comprehensive analysis of lymph node stroma-expressed Ig superfamily members reveals redundant and nonredundant roles for ICAM-1, ICAM-2, and VCAM-1 in lymphocyte homing. *Blood* 116, 915–925 (2010).

26. B. Stolp, F. Thelen, X. Ficht, L. M. Altenburger, N. Ruef, V. V. G. K. Inavalli, P. Germann, N. Page, F. Moalli, A. Raimondi, K. A. Keyser, S. M. S. Jafari, F. Barone, M. S. Dettmer, D. Merkler, M. Iannacone, J. Sharpe, C. Schlapbach, O. T. Fackler, U. V. Nägerl, J. V. Stein, Salivary gland macrophages and tissue-resident CD8+ T cells cooperate for homeostatic organ surveillance. *Sci Immunol* 5, eaaz4371 (2020).

27. C. E. Hughes, R. J. B. Nibbs, A guide to chemokines and their receptors. *FEBS J* 285, 2944–2971 (2018).

28. A. Reversat, F. Gaertner, J. Merrin, J. Stopp, S. Tasciyan, J. Aguilera, I. de Vries, R. Hauschild, M. Hons, M. Piel, A. Callan-Jones, R. Voituriez, M. Sixt, Cellular locomotion using environmental topography. *Nature* 582, 582–585 (2020).

29. A. J. Lomakin, C. J. Cattin, D. Cuvelier, Z. Alraies, M. Molina, G. P. F. Nader, N. Srivastava, P. J. Sáez, J. M. Garcia-Arcos, I. Y. Zhitnyak, A. Bhargava, M. K. Driscoll, E. S. Welf, R. Fiolka, R. J. Petrie, N. S. D. Silva, J. M. González-Granado, N. Manel, A. M. Lennon-Duménil, D. J. Müller, M. Piel, The nucleus acts as a ruler tailoring cell responses to spatial constraints. *Science* 370, eaba2894 (2020).

30. V. Venturini, F. Pezzano, F. C. Castro, H.-M. Häkkinen, S. Jiménez-Delgado, M. Colomer-Rosell, M. Marro, Q. Tolosa-Ramon, S. Paz-López, M. A. Valverde, J. Weghuber, P. Loza-Alvarez, M. Krieg, S. Wieser, V. Ruprecht, The nucleus measures shape changes for cellular proprioception to control dynamic cell behavior. *Science* 370, eaba2644 (2020).

31. K. A. Hogquist, S. C. Jameson, W. R. Heath, J. L. Howard, M. J. Bevan, F. R. Carbone, T cell receptor antagonist peptides induce positive selection. *Cell* 76, 17–27 (1994).

32. S. M. Kallert, S. Darbre, W. V. Bonilla, M. Kreutzfeldt, N. Page, P. Müller, M. Kreuzaler, M. Lu, S. Favre, F. Kreppel, M. Löhning, S. A. Luther, A. Zippelius, D. Merkler, D. D. Pinschewer, Replicating viral vector platform exploits alarmin signals for potent CD8+ T cell-mediated tumour immunotherapy. *Nat Commun* 8, 15327 (2017).

33. J. Riedl, A. H. Crevenna, K. Kessenbrock, J. H. Yu, D. Neukirchen, M. Bista, F. Bradke, D. Jenne, T. A. Holak, Z. Werb, M. Sixt, R. Wedlich-Söldner, Lifeact: a versatile marker to visualize F-actin. *Nat Meth* 5, 605–607 (2008).

34. A. Babich, S. Li, R. S. O'Connor, M. C. Milone, B. D. Freedman, J. K. Burkhardt, F-actin polymerization and retrograde flow drive sustained PLCγ1 signaling during T cell activation. *J Cell Biol* 197, 775–787 (2012).

35. A. T. Ritter, Y. Asano, J. C. Stinchcombe, N. M. G. Dieckmann, B.-C. Chen, C. Gawden-Bone, S. van Engelenburg, W. Legant, L. Gao, M. W. Davidson, E. Betzig, J. Lippincott-Schwartz, G. M. Griffiths, Actin Depletion Initiates Events Leading to Granule Secretion at the Immunological Synapse. *Immunity* 42, 864–876 (2015).

36. W. A. Comrie, A. Babich, J. K. Burkhardt, F-actin flow drives affinity maturation and spatial organization of LFA-1 at the immunological synapse. *J Cell Biol* 208, 475–491 (2015).

37. M. Bajénoff, J. G. Egen, L. Y. Koo, J. P. Laugier, F. Brau, N. Glaichenhaus, R. N. Germain, Stromal Cell Networks Regulate Lymphocyte Entry, Migration, and Territoriality in Lymph Nodes. *Immunity* 25, 989–1001 (2006).

38. J. Renkawitz, K. Schumann, M. Weber, T. Lämmermann, H. Pflicke, M. Piel, J. Polleux, J. P. Spatz, M. Sixt, Adaptive force transmission in amoeboid cell migration. *Nat Cell Biol* 11, 1438–1443 (2009).

39. D. Bray, J. G. White, Cortical Flow in Animal Cells. *Science* 239, 883–888 (1988).

40. Y. Fukui, O. Hashimoto, T. Sanui, T. Oono, H. Koga, M. Abe, A. Inayoshi, M. Noda, M. Oike, T. Shirai, T. Sasazuki, Haematopoietic cell-specific CDM family protein DOCK2 is essential for lymphocyte migration. *Nature* 412, 826–831 (2001).

41. A. Leithner, A. Eichner, J. Müller, A. Reversat, M. Brown, J. Schwarz, J. Merrin, D. J. J. de Gorter, F. Schur, J. Bayerl, I. de Vries, S. Wieser, R. Hauschild, F. P. L. Lai, M. Moser, D. Kerjaschki, K. Rottner, J. V. Small, T. E. B. Stradal, M. Sixt, Diversified actin protrusions promote environmental exploration but are dispensable for locomotion of leukocytes. *Nat Cell Biol* 18, 1253–1259 (2016).

42. P. Vargas, P. Maiuri, M. Bretou, P. J. Sáez, P. Pierobon, M. Maurin, M. Chabaud, D. Lankar, D. Obino, E. Terriac, M. Raab, H.-R. Thiam, T. Brocker, S. M. Kitchen-Goosen, A. S. Alberts, P. Sunareni, S. Xia, R. Li, R. Voituriez, M. Piel, A.-M. Lennon-Duménil, Innate control of actin nucleation determines two distinct migration behaviours in dendritic cells. *Nat Cell Biol* 18, 43–53 (2016).

43. L. K. Fritz-Laylin, S. J. Lord, R. D. Mullins, WASP and SCAR are evolutionarily conserved in actin-filled pseudopod-based motility. *J Cell Biol* 216, 1673–1688 (2017).

44. A. Nishikimi, T. Uruno, X. Duan, Q. Cao, Y. Okamura, T. Saitoh, N. Saito, S. Sakaoka, Y. Du, A. Suenaga, M. Kukimoto-Niino, K. Miyano, K. Gotoh, T. Okabe, F. Sanematsu, Y. Tanaka, H. Sumimoto, T. Honma, S. Yokoyama, T. Nagano, D. Kohda, M. Kanai, Y. Fukui, Blockade of Inflammatory Responses by a Small-Molecule Inhibitor of the Rac Activator DOCK2. *Chem Biol* 19, 488–497 (2012).

45. B. J. Nolen, N. Tomasevic, A. Russell, D. W. Pierce, Z. Jia, C. D. McCormick, J. Hartman, R. Sakowicz, T. D. Pollard, Characterization of two classes of small molecule inhibitors of Arp2/3 complex. *Nature* 460, 1031–1034 (2009).

46. H. Jiang, F. Pan, L. M. Erickson, M.-S. Jang, T. Sanui, Y. Kunisaki, T. Sasazuki, M. Kobayashi, Y. Fukui, Deletion of DOCK2, a regulator of the actin cytoskeleton in lymphocytes, suppresses cardiac allograft rejection. *J Exp Medicine* 202, 1121–1130 (2005).

47. Q. Zhang, C. G. Dove, J. L. Hor, H. M. Murdock, D. M. Strauss-Albee, J. A. Garcia, J. N. Mandl, R. A. Grodick, H. Jing, D. B. Chandler-Brown, T. E. Lenardo, G. Crawford, H. F. Matthews, A. F. Freeman, R. J. Cornall, R. N. Germain, S. N. Mueller, H. C. Su, DOCK8 regulates lymphocyte shape integrity for skin antiviral immunity. *J. Exp. Med.* 211, 2549–2566 (2014).

48. K. M. Yamada, M. Sixt, Mechanisms of 3D cell migration. *Nat Rev Mol Cell Bio* 20, 738–752 (2019).

49. Y. Zhang, M. A. Conti, D. Malide, F. Dong, A. Wang, Y. A. Shmist, C. Liu, P. Zerfas, M. P. Daniels, C.-C. Chan, E. Kozin, B. Kachar, M. J. Kelley, J. B. Kopp, R. S. Adelstein, Mouse models of MYH9-related disease: mutations in nonmuscle myosin II-A. *Blood* 119, 238–250 (2012).

50. A. Zehrer, R. Pick, M. Salvermoser, A. Boda, M. Miller, K. Stark, L. T. Weckbach, B. Walzog, D. Begandt, A Fundamental Role of Myh9 for Neutrophil Migration in Innate Immunity. *The Journal of Immunology* 201, 1748–1764 (2018).

51. M. Vicente-Manzanares, X. Ma, R. S. Adelstein, A. R. Horwitz, Non-muscle myosin II takes centre stage in cell adhesion and migration. *Nat Rev Mol Cell Bio* 10, 778–790 (2009).

52. T. Isogai, R. van der Kammen, M. Innocenti, SMIFH2 has effects on Formins and p53 that perturb the cell cytoskeleton. *Sci Rep* 5, 9802–15 (2015).

53. Y. Nishimura, S. Shi, F. Zhang, R. Liu, Y. Takagi, A. D. Bershadsky, V. Viasnoff, J. R. Sellers, The Formin Inhibitor, SMIFH2, Inhibits Members of the Myosin Superfamily. *J Cell Sci* 134, jcs.253708 (2021).

54. T. F. Robertson, P. Chengappa, D. G. Atria, C. F. Wu, L. Avery, N. H. Roy, I. Maillard, R. J. Petrie, J. K. Burkhardt, Lymphocyte egress signal sphingosine-1-phosphate promotes ERM-guided, bleb-based migration. *J Cell Biol* 220, e202007182 (2021).

55. P. Kameritsch, J. Renkawitz, Principles of Leukocyte Migration Strategies. *Trends in Cell Biology* 30, 818–832 (2020).

56. A. Smith, P. Stanley, K. Jones, L. Svensson, A. McDowall, N. Hogg, The role of the integrin LFA-1 in T-lymphocyte migration. *Immunol Rev* 218, 135–146 (2009).

57. T. Wolf, W. Jin, G. Zoppi, I. A. Vogel, M. Akhmedov, C. K. E. Bleck, T. Beltraminelli, J. C. Rieckmann, N. J. Ramirez, M. Benevento, S. Notarbartolo, D. Bumann, F. Meissner, B. Grimbacher, M. Mann, A. Lanzavecchia, F. Sallusto, I. Kwee, R. Geiger, Dynamics in protein translation sustaining T cell preparedness. *Nat Immunol* 21, 927–937 (2020).

58. A. D. Weems, E. S. Welf, M. K. Driscoll, F. Y. Zhou, H. Mazloom-Farsibaf, B.-J. Chang, V. S. Murali, G. M. Gihana, B. G. Weiss, J. Chi, D. Rajendran, K. M. Dean, R. Fiolka, G. Danuser, Blebs promote cell survival by assembling oncogenic signalling hubs. *Nature* 615, 517–525 (2023).

59. A. Smith, Y. R. Carrasco, P. Stanley, N. Kieffer, F. D. Batista, N. Hogg, A talin-dependent LFA-1 focal zone is formed by rapidly migrating T lymphocytes. *J Cell Biology* 170, 141–151 (2005).

60. P. R. O'Neill, J. A. Castillo-Badillo, X. Meshik, V. Kalyanaraman, K. Melgarejo, N. Gautam, Membrane Flow Drives an Adhesion-Independent Amoeboid Cell Migration Mode. *Dev Cell* 46, 9-22.e4 (2018).

61. L. Aoun, A. Farutin, N. Garcia-Seyda, P. Nègre, M. S. Rizvi, S. Tlili, S. Song, X. Luo, M. Biarnes-Pelicot, R. Galland, J.-B. Sibarita, A. Michelot, C. Hivroz, S. Rafai, M.-P. Valignat, C. Misbah, O. Theodoly, Amoeboid Swimming Is Propelled by Molecular Paddling in Lymphocytes. *Biophys J* 119, 1157–1177 (2020).

62. A. Saha, M. Nishikawa, M. Behrndt, C.-P. Heisenberg, F. Jülicher, S. W. Grill, Determining Physical Properties of the Cell Cortex. *Biophysical Journal* 110, 1421–1429 (2016).

63. B. Enyedi, M. Jelcic, P. Niethammer, The Cell Nucleus Serves as a Mechanotransducer of Tissue Damage-Induced Inflammation. *Cell* 165, 1160–1170 (2016).

64. A. Selezneva, A. J. Gibb, D. Willis, The Nuclear Envelope as a Regulator of Immune Cell Function. *Front. Immun.* , 1–10 (2022).

65. M. Tymianski, M. C. Wallace, I. Spigelman, M. Uno, P. L. Carlen, C. H. Tator, M. P. Charlton, Cell-permeant Ca2+ chelators reduce early excitotoxic and ischemic neuronal injury in vitro and in vivo. *Neuron* 11, 221–235 (1993).

66. Z. Shen, P. Niethammer, A cellular sense of space and pressure. *Science* 370, 295–296 (2020).

67. J. T. Long, J. Lammerding, Nuclear Deformation Lets Cells Gauge Their Physical Confinement. *Dev Cell* 56, 156–158 (2021).

68. R. D. Mullins, P. Bieling, D. A. Fletcher, From solution to surface to filament: actin flux into branched networks. *Biophys Rev* 10, 1537–1551 (2018).

69. L. K. Mackay, A. Rahimpour, J. Z. Ma, N. Collins, A. T. Stock, M.-L. Hafon, J. Vega-Ramos, P. Lauzurica, S. N. Mueller, T. Stefanovic, D. C. Tscharke, W. R. Heath, M. Inouye, F. R. Carbone, T. Gebhardt, The developmental pathway for CD103+CD8+ tissue-resident memory T cells of skin. *Nat. Immunol.* 14, 1294–1301 (2013).

70. M. Huse, Mechanical forces in the immune system. *Nat Rev Immunol* 17, 679–690 (2017).

71. S. V. Pageon, M. A. Govendir, D. Kempe, M. Biro, Mechanoimmunology: molecular-scale forces govern immune cell functions. *Mol Biol Cell* 29, 1919–1926 (2018).

72. M. Chabaud, N. Paillon, K. Gaus, C. Hivroz, Mechanobiology of antigen-induced T cell arrest. *Biol. Cell* (2020), doi:10.1111/boc.201900093.

73. H. Du, J. M. Bartleson, S. Butenko, V. Alonso, W. F. Liu, D. A. Winer, M. J. Butte, Tuning immunity through tissue mechanotransduction. *Nat Rev Immunol* 23, 174–188 (2023).

74. R. Basu, B. M. Whitlock, J. Husson, A. L. Floc'h, W. Jin, A. Oyler-Yaniv, F. Dotiwala, G. Giannone, C. Hivroz, N. Biais, J. Lieberman, L. C. Kam, M. Huse, Cytotoxic T Cells Use Mechanical Force to Potentiate Target Cell Killing. *Cell* 165, 100–110 (2016).

75. M. Tello-Lafoz, K. Srpan, E. E. Sanchez, J. Hu, J. Remsik, Y. Romin, A. Calò, D. Hoen, U. Bhanot, L. Morris, A. Boire, K. C. Hsu, J. Massagué, M. Huse, E. E. Er, Cytotoxic lymphocytes target characteristic biophysical vulnerabilities in cancer. *Immunity* 54, 1037-1054.e7 (2021).

1013 76. A. G. Solis, P. Bielecki, H. R. Steach, L. Sharma, C. C. D. Harman, S. Yun, M. R. de Zoete, J.
1014 N. Warnock, S. D. F. To, A. G. York, M. Mack, M. A. Schwartz, Charles. S. D. Cruz, N. W. Palm, R.
1015 Jackson, R. A. Flavell, Mechanosensation of cyclical force by PIEZO1 is essential for innate
1016 immunity. *Nature* 573, 69–74 (2019).

1017 77. D. Liu, L. Duan, L. B. Rodda, E. Lu, Y. Xu, J. An, L. Qiu, F. Liu, M. R. Looney, Z. Yang, C. D.
1018 C. Allen, Z. Li, A. Marson, J. G. Cyster, CD97 promotes spleen dendritic cell homeostasis through
1019 the mechanosensing of red blood cells. *Science* 375, eabi5965 (2022).

1020 78. H. D. Moreau, M. Piel, R. Voituriez, A.-M. Lennon-Duménil, Integrating Physical and Molecular
1021 Insights on Immune Cell Migration. *Trends Immunol* 39, 632–643 (2018).

1022 79. S. van Helvert, C. Storm, P. Friedl, Mechanoreciprocity in cell migration. *Nat Cell Biol* 20, 8–20
1023 (2018).

1024 80. F. Moalli, X. Ficht, P. Germann, M. Vladymyrov, B. Stolp, I. de Vries, R. Lyck, J. Balmer, A.
1025 Fiocchi, M. Kreutzfeldt, D. Merkler, M. Iannacone, A. Ariga, M. H. Stoffel, J. Sharpe, M. Bähler, M.
1026 Sixt, A. Diz-Muñoz, J. V. Stein, The Rho regulator Myosin IXb enables nonlymphoid tissue seeding
1027 of protective CD8+ T cells. *J. Exp. Medicine* 215, 1869–1890 (2018).

1028 81. T. Lämmermann, B. L. Bader, S. J. Monkley, T. Worbs, R. Wedlich-Söldner, K. Hirsch, M.
1029 Keller, R. Förster, D. R. Critchley, R. Fässler, M. Sixt, Rapid leukocyte migration by integrin-
1030 independent flowing and squeezing. *Nature* 453, 51–55 (2008).

1031 82. J. Renkawitz, A. Kopf, J. Stopp, I. de Vries, M. K. Driscoll, J. Merrin, R. Hauschild, E. S. Welf,
1032 G. Danuser, R. Fiolka, M. Sixt, Nuclear positioning facilitates amoeboid migration along the path of
1033 least resistance. *Nature* 568, 546–550 (2019).

1034 83. Y. Kalukula, A. D. Stephens, J. Lammerding, S. Gabriele, Mechanics and functional
1035 consequences of nuclear deformations. *Nat Rev Mol Cell Bio* , 1–20 (2022).

1036 84. B. Enyedi, P. Niethammer, A Case for the Nuclear Membrane as a Mechanotransducer. *Cell*
1037 *Mol Bioeng* 9, 247–251 (2016).

1038 85. J. B. Park, C. S. Lee, J.-H. Jang, J. Ghim, Y.-J. Kim, S. You, D. Hwang, P.-G. Suh, S. H. Ryu,
1039 Phospholipase signalling networks in cancer. *Nat Rev Cancer* 12, 782–792 (2012).

1040 86. C. C. Leslie, Cytosolic phospholipase A_2: physiological function and role in disease. *J Lipid Res*
1041 56, 1386–1402 (2015).

1042 87. F. Fenninger, W. A. Jefferies, What's Bred in the Bone: Calcium Channels in Lymphocytes.
1043 *The Journal of Immunology* 202, 1021–1030 (2019).

1044 88. Z. Alraies, C. A. Rivera, M.-G. Delgado, D. Sanséau, M. Maurin, R. Amadio, G. M. Piperno, G.
1045 Dunsmore, A. Yatim, L. L. Mariano, P. J. Sáez, M. Gratia, O. Lamiable, A. Moreau, A. Williart, B.
1046 Albaud, P. Legoix, H. Nakano, D. N. Cook, T. Lawrence, N. Manel, F. Benvenuti, F. Ginhoux, H. D.
1047 Moreau, G. P. F. Nader, M. Piel, A.-M. Lennon-Duménil, An Arp2/3-cPLA2-NFκB axis acts as a
1048 Cell Shape Sensor to drive Homeostatic Migration of Dendritic Cells. *Biorxiv* , 2022.08.09.503223
1049 (2022).

1050 89. B. C. Schaefer, M. L. Schaefer, J. W. Kappler, P. Marrack, R. M. Kedl, Observation of Antigen-
1051 Dependent CD8+ T-Cell/ Dendritic Cell Interactions in Vivo. *Cell Immunol* 214, 110–122 (2001).

1052 90. A. C. Kirby, M. C. Coles, P. M. Kaye, Alveolar Macrophages Transport Pathogens to Lung
1053 Draining Lymph Nodes. *J Immunol* 183, 1983–1989 (2009).

91. W. N. de Vries, L. T. Binns, K. S. Fancher, J. Dean, R. Moore, R. Kemler, B. B. Knowles, Expression of Cre recombinase in mouse oocytes: A means to study maternal effect genes . *Genesis* 26, 110–112 (2000).

92. L. Madisen, T. A. Zwingman, S. M. Sunkin, S. W. Oh, H. A. Zariwala, H. Gu, L. L. Ng, R. D. Palmiter, M. J. Hawrylycz, A. R. Jones, E. S. Lein, H. Zeng, A robust and high-throughput Cre reporting and characterization system for the whole mouse brain. *Nat. Neurosci.* 13, 133–140 (2010).

93. M. D. Muzumdar, B. Tasic, K. Miyamichi, L. Li, L. Luo, A global double-fluorescent Cre reporter mouse. *Genesis* 45, 593–605 (2007).

94. J. Jacobelli, R. S. Friedman, M. A. Conti, A.-M. Lennon-Dumenil, M. Piel, C. M. Sorensen, R. S. Adelstein, M. F. Krummel, Confinement-optimized three-dimensional T cell amoeboid motility is modulated via myosin IIA–regulated adhesions. *Nat Immunol* 11, 953–961 (2010).

95. Y. Harada, Y. Tanaka, M. Terasawa, M. Pieczyk, K. Habiro, T. Katakai, K. Hanawa-Suetsugu, M. Kukimoto-Niino, T. Nishizaki, M. Shirouzu, X. Duan, T. Uruno, A. Nishikimi, F. Sanematsu, S. Yokoyama, J. V. Stein, T. Kinashi, Y. Fukui, DOCK8 is a Cdc42 activator critical for interstitial dendritic cell migration during immune responses. *Blood* 119, 4451–4461 (2012).

96. Y. Kunisaki, A. Nishikimi, Y. Tanaka, R. Takii, M. Noda, A. Inayoshi, K. Watanabe, F. Sanematsu, T. Sasazuki, T. Sasaki, Y. Fukui, DOCK2 is a Rac activator that regulates motility and polarity during neutrophil chemotaxis. *J Cell Biology* 174, 647–652 (2006).

97. X. Ficht, F. Thelen, B. Stolp, J. V. Stein, Preparation of Murine Submandibular Salivary Gland for Upright Intravital Microscopy. *J Vis Exp* 215, 1869–1890 (2018).

98. M. Vladymyrov, J. Abe, F. Moalli, J. V. Stein, A. Ariga, Real-time tissue offset correction system for intravital multiphoton microscopy. *Journal of Immunological Methods* 438, 35–41 (2016).

99. J. Daniel, A. G. Godin, M. Palayret, B. Lounis, L. Cognet, M. Blanchard-Desce, Innovative molecular-based fluorescent nanoparticles for multicolor single particle tracking in cells. *J. Phys. D: Appl. Phys.* 49, 084002 (2016).

100. D. J. Barry, C. H. Durkin, J. V. Abella, M. Way, Open source software for quantification of cell migration, protrusions, and fluorescence intensities. *J Cell Biol* 209, 163–180 (2015).

101. E. U. Allmen, G. P. B. Samson, V. Purvanov, T. Maeda, D. F. Legler, CAL-1 as Cellular Model System to Study CCR7-Guided Human Dendritic Cell Migration. *Front Immunol* 12, 702453 (2021).

102. S. Halle, K. A. Keyser, F. R. Stahl, A. Busche, A. Marquardt, X. Zheng, M. Galla, V. Heissmeyer, K. Heller, J. Boelter, K. Wagner, Y. Bischoff, R. Martens, A. Braun, K. Werth, A. Uvarovskii, H. Kempf, M. Meyer-Hermann, R. Arens, M. Kremer, G. Sutter, M. Messerle, R. Förster, In Vivo Killing Capacity of Cytotoxic T Cells Is Limited and Involves Dynamic Interactions and T Cell Cooperativity. *Immunity* 44, 233–245 (2016).

Acknowledgments

We thank M. Sixt for critical feedback on the manuscript.

Funding

This work was funded by Swiss National Foundation (SNF) project grants 31003A_172994, 310030L_197711, 310030_200406, Sinergia project grant CRSII5_170969 (to JVS), Leopoldina fellowship LPDS 2011-16 and the Deutsche Forschungsgemeinschaft project number 240245660-SFB1129 (project 8) (to BS). This work benefitted from the BioImage Light Microscopy Facility and Cell Analytics Facility of the University of Fribourg.

Author contributions

NR and JMM performed most experiments and analysis with help from XF, VP, SW, PP, BS, FT and JBdA. MP wrote the script for morphometric analysis and PG provided scripts for *in vivo* cell tracking. JA, JS, DFL and JVS supervised the work. JVS wrote the manuscript with input by all coauthors.

Competing interests

The authors declare no competing interests.

Data and materials availability

All data needed to evaluate the conclusions in the paper are present in the paper or the Supplementary Materials.

Figure legends

Figure 1. SMG T_{RM} autonomously generate F-actin flow for chemokine- and specific adhesion-independent amoeboid motility. A. Experimental layout. **B.** Flow cytometry plots and quantification of F-actin content in LN and spleen (Spl) T_N, T_{CM}, T_{EM} and SMG T_{RM}. Bars represent median. **C.** TIRF images of cortical F-actin flow in LifeAct-GFP$^+$ T_N and SMG T_{RM} under agarose. Note that for T_N plated in the absence of chemokine (- CK), there is no front or rear discernible, since these cells are non-polarized. Yellow lines indicate rearward (continuous) and forward (dotted) F-actin flow. CK, chemokine; HSA, human serum albumin. **D.** Global F-actin flow speeds in T_N and SMG T_{RM}. **E.** Schematic layout of dynamic and morphometric analysis. Scale bar, 10 µm. **F.** Wide-field fluorescence microscopy images of T_N and SMG T_{RM} under agarose migration. Time in min:s; Scale bar, 10 µm. **G.** Dynamic and morphometric analysis of T_N and SMG T_{RM} displacement. Data in B and G were pooled from at least two independent experiments with n = 11-12 mice (B) and n = 60-279 tracks per condition (G), and D is from one of two representative experiments with 21-24 cells per condition and n = 411-777 individual F-actin spots tracked per condition (except T_N + CK on ICAM-1: 144 F-actin spots).Statistical analysis was done by a Kruskal-Wallis test against LN T_N (B) or between all columns (D, G). **, $p < 0.01$; ***, $p < 0.001$.

Figure 2. SMG T_{RM} display high constitutive actomyosin contractility and bleb formation during spontaneous migration. A. Flow cytometry analysis of MYH9-GFP-expressing T_{CM}, T_{EM} and SMG T_{RM} DsRed$^+$ OT-I T cells. **B.** MYH9-GFP dynamics in DsRed$^+$ OT-I T cells under agarose migration. Empty arrowhead indicates leading edge protrusion. Time in min:s; Scale bar, 10 µm. **C.** Flow cytometry analysis of pMLC in endogenous T_N and OT-I T_{CM}, T_{EM} and SMG T_{RM}. **D.** Immunofluorescent analysis of pMLC in spleen and SMG memory OT-I T cells. **E.** Scheme of Rho-triggered pMLC generation and selected inhibitors. **F.** Wide-field fluorescence microscopy images of SMG T_{RM} under agarose migration in presence of inhibitors. Time in min:s; Scale bar, 10 µm. **G.** Dynamic and morphometric analysis of SMG T_{RM} displacement. **H.** Scheme of F-actin-filled protrusion versus bleb formation in migrating LifeAct-GFP x mT/mG SMG T_{RM}. **I.** High temporal resolution protrusion analysis of migrating LifeAct-GFP x mT/mG SMG T_{RM} OT-I under 2D and 3D confinement. Empty arrowheads indicate F-actin-filled protrusions, filled arrowheads indicate

1144 blebs. Scale bar, 10 µm. Bars in A and C represent median. Data in A (n = 6 mice), C (n = 9-11
1145 mice), D (n = 63-65 cells), and G (n = 184-239 tracks) were pooled from at least two independent
1146 experiments and analyzed by ANOVA (A, C), Mann-Whitney test (D) or a Kruskal-Wallis test
1147 against control (G). *, $p < 0.05$; **, $p < 0.01$; ***, $p < 0.001$.
1148
1149 **Figure 3. Exocrine gland T_{RM} react to mechanical load of their environment with motility. A.**
1150 Experimental layout. **B.** Wide-field fluorescence microscopy images of SMG T_{RM} migrating without
1151 or with confinement. **C.** Exemplary tracks. **D.** Dynamic and morphometric analysis of T_{RM} motility
1152 with or without confinement. Scale bar, 10 µm. **E.** Exemplary tracks and wide-field fluorescence
1153 microscopy images of SMG T_{RM} migrating under distinct mechanical load. Scale bar, 5 µm. **F.**
1154 Dynamic and morphometric analysis of T_{RM} motility under distinct mechanical load. **G, H.**
1155 Exemplary tracks (G) and dynamic and morphometric analysis of lacrimal gland (LG) and small
1156 intestine (SI) T_{RM} motility (H) on HSA-coated plates under confinement. Data in D (n = 454-1000
1157 tracks), F (n = 159-323 tracks) and H (n = 68-242 tracks) were pooled from at least two
1158 independent experiments and analyzed using a Student's t-test or Mann-Whitney test (D, H) or a
1159 Kruskal-Wallis test between all columns (F). *, $p < 0.05$; **, $p < 0.01$; ***, $p < 0.001$.
1160
1161 **Figure 4. Confinement-induced nuclear deformation correlates with Ca^{2+} and AA-dependent**
1162 **autonomous SMG T_{RM} motility. A.** Confocal image of nuclear deformation in under agarose
1163 confinement. Scale bar, 5 µm. **B.** Projected maximum cross-section area and maximum nuclear
1164 height with and without confinement (n = 20-23 nuclei). **C.** Schematic layout, micrograph and
1165 exemplary tracks of SMG T_{RM} in confinement chamber. Scale bar, 5 µm. **D.** Dynamic and
1166 morphometric analysis of T_{RM} motility in confinement chambers. **E.** Scheme of confinement-
1167 induced nuclear stretching and selected inhibitors of "evasive reflex" mediated by Ca^{2+} flux from
1168 intracellular stores, induction of PLA2 activity and release of arachidonic acid (AA). 2APB, BAPTA-
1169 AM and the AA analogue AACOCF3 are inhibitors of intracellular Ca^{2+} channels, intracellular Ca^{2+}
1170 and PLA2 activity, respectively. **F.** Wide-field fluorescence microscopy images of SMG T_{RM} under
1171 agarose migration in presence of AACOCF3 and AA. Time in min:s; Scale bar, 10 µm. **G.** Dynamic
1172 and morphometric analysis of T_{RM} motility in presence of AACOCF3 and AA. **H.** Wide-field

fluorescence microscopy images of SMG T_{RM} under agarose migration in presence of BAPTA-AM and 2ABP. Time in min:s; Scale bar, 10 µm. **I.** Dynamic and morphometric analysis of T_{RM} motility under agarose in presence of BAPTA-AM and 2ABP. Data in D (n = 35-43 tracks), G (n = 296-708 tracks) and I (n = 63-199 tracks) were pooled from at least two independent experiments and analyzed using Student's t-test and Mann-Whitney test (D), or Kruskal-Wallis against control (G, I). *, $p < 0.05$; **, $p < 0.01$; ***, $p < 0.001$.

Figure 5. Blocking mechanosensing impairs T_{RM} target cell identification. A. Experimental layout. **B.** Wide-field fluorescence microscopy images of confined SMG T_{RM} tracking of dispersed target cells with and without AACOCF3. Time in min:s; scale bar, 30 µm. **C.** Quantification of T_{RM} – target B cell synapse formation with or without AACOCF3. Data in C (n = 139-341 synapses) were pooled from two independent experiments and analyzed by Mann-Whitney test. *, $p < 0.05$.

Figure 6. Blocking mechanosensing disrupts *in vivo* SMG T_{RM} migration. A. Confocal image of SMG T_{RM} (arrowhead) *in situ*. Scale bar, 5 µm. **B.** Scheme of BAPTA-AM superfusion. **C.** 2PM images of SMG T_{RM} migration before (baseline) and after 50 µM BAPTA-AM superfusion. Scale bar, 10 µM. **D-G.** Speeds (D), meandering index (E), arrest coefficient (F) and sphericity (G) of T_{RM} before and 1-4 h after superfusion with BAPTA-AM. **H.** Experimental layout of MCMV-3D-ΔvRAP rechallenge. **I.** Confocal sections of MCMV-challenged SMG in control (DMSO)-and AACOCF3-treated recipients. Dotted line marks outline of SMG section, square depicts insert. Scale bar, 500 and 50 (insert) µm. **J.** Number of T_{RM} per area in control- and AACOCF3-treated SMG. **K.** Percent of clustered T_{RM} in control-and AACOCF3-treated recipients in 10-14 sections from 3 independent experiments (n = 24 control- and AACOCF3-treated mice in total). **L.** Graphical summary. Data in D-G (n = 207-323 tracks), J and K are pooled from at least two experiments and analyzed using Kruskal-Wallis (D-G), Student's t-test (J) or Mann-Whitney test (K). *, $p < 0.05$; **, $p < 0.01$; ***, $p < 0.001$.

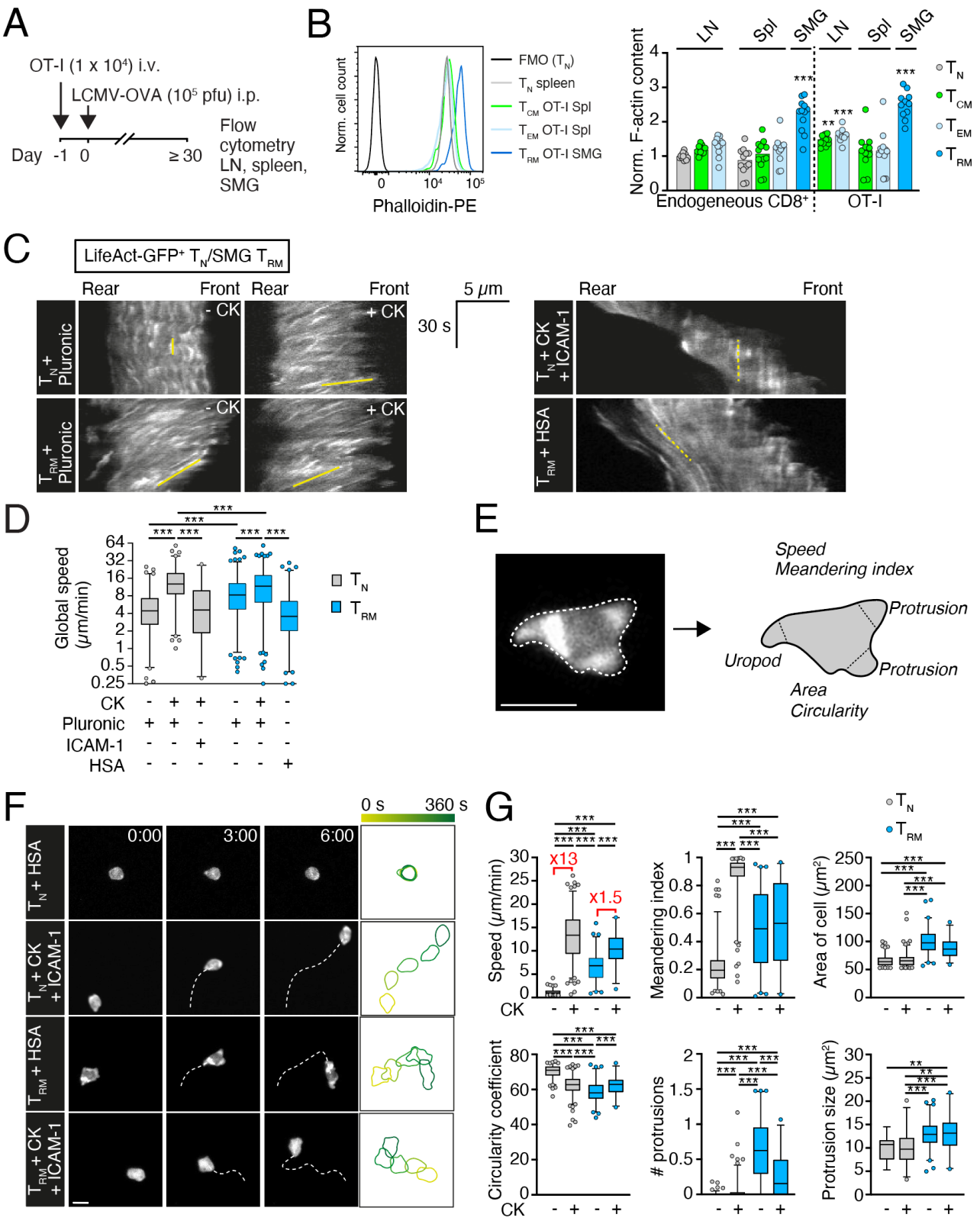
A
OT-I (1 x 10⁴) i.v.
LCMV-OVA (10⁵ pfu) i.p.
Day -1 0 ≥ 30
Flow cytometry LN, spleen, SMG
B
Norm. cell count
Phalloidin-PE
FMO (T_N)
T_N spleen
T_CM OT-I Spl
T_EM OT-I Spl
T_RM OT-I SMG
Norm. F-actin content
LN
Spl
SMG
Endogeneous CD8⁺
OT-I
T_N
T_CM
T_EM
T_RM
C
LifeAct-GFP⁺ T_N/SMG T_RM
Rear
Front
- CK
+ CK
5 μm
30 s
T_N + Pluronic
T_RM + Pluronic
T_N + CK + ICAM-1
T_RM + HSA
D
Global speed (μm/min)
CK
Pluronic
ICAM-1
HSA
E
Speed
Meandering index
Protrusion
Uropod
Area
Circularity
F
0 s
360 s
0:00
3:00
6:00
G
Speed (μm/min)
x13
x1.5
Meandering index
Area of cell (μm²)
Circularity coefficient
protrusions
Protrusion size (μm²)

Figure 1

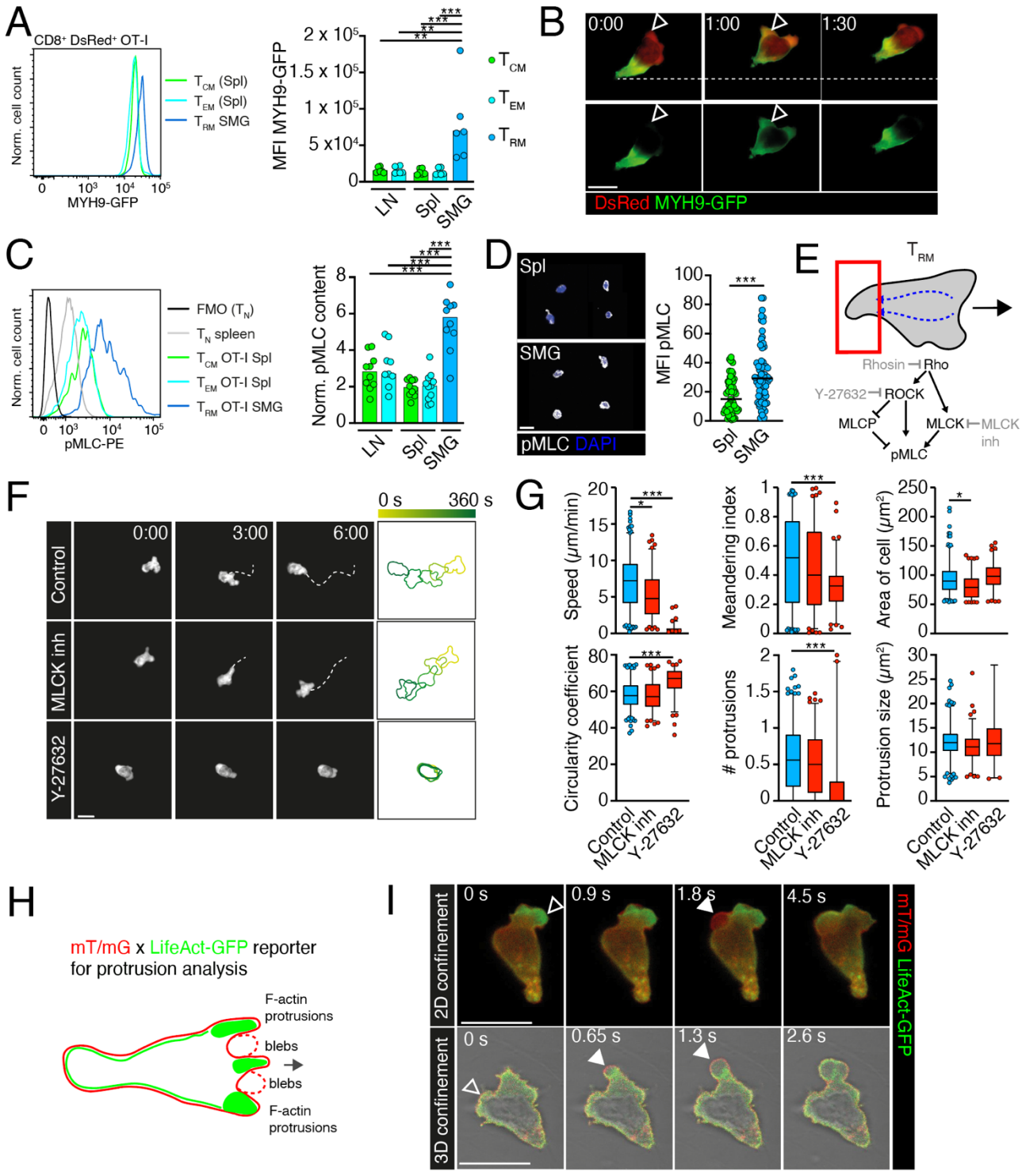
A
CD8+ DsRed+ OT-I
Norm. cell count
MYH9-GFP
TCM (Spl)
TEM (Spl)
TRM SMG
MFI MYH9-GFP
LN
Spl
SMG
TCM
TEM
TRM
B
0:00
1:00
1:30
DsRed MYH9-GFP
C
FMO (TN)
TN spleen
TCM OT-I Spl
TEM OT-I Spl
TRM OT-I SMG
pMLC-PE
Norm. pMLC content
D
Spl
SMG
pMLC DAPI
MFI pMLC
E
TRM
Rhosin
Rho
Y-27632
ROCK
MLCP
MLCK
MLCK inh
pMLC
F
0 s
360 s
0:00
3:00
6:00
Control
MLCK inh
Y-27632
G
Speed (μm/min)
Meandering index
Area of cell (μm²)
Circularity coefficient
protrusions
Protrusion size (μm²)
Control
MLCK inh
Y-27632
H
mT/mG x LifeAct-GFP reporter
for protrusion analysis
F-actin
protrusions
blebs
blebs
F-actin
protrusions
I
2D confinement
3D confinement
0 s
0.9 s
1.8 s
4.5 s
0 s
0.65 s
1.3 s
2.6 s
mT/mG LifeAct-GFP

Figure 2

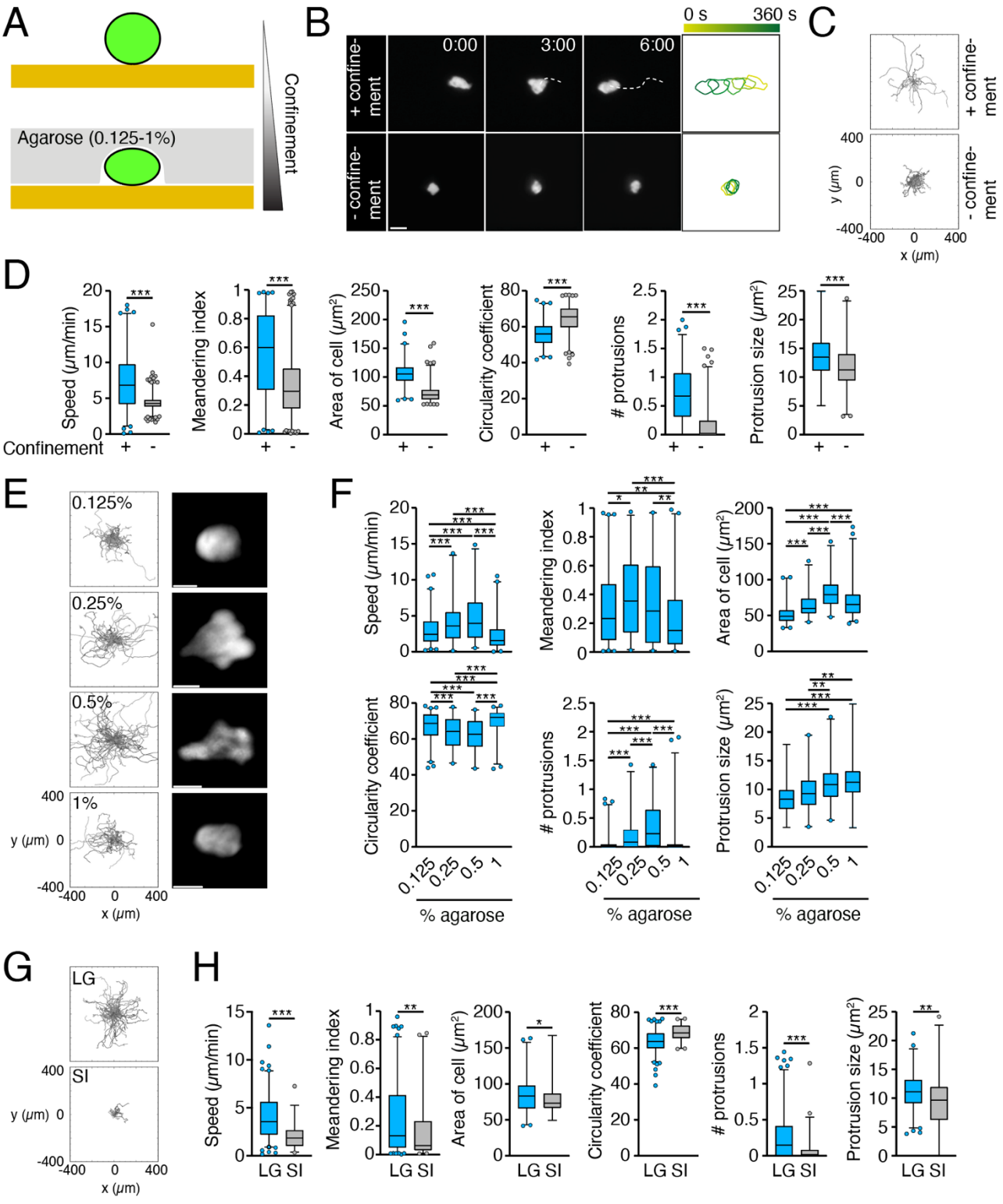
A
Agarose (0.125-1%)
Confinement
B
0 s
360 s
+ confine-ment
- confine-ment
0:00
3:00
6:00
C
+ confine-ment
- confine-ment
400
0
-400
y (μm)
x (μm)
D
Speed (μm/min)
Meandering index
Area of cell (μm²)
Circularity coefficient
protrusions
Protrusion size (μm²)
Confinement
+
-
E
0.125%
0.25%
0.5%
1%
y (μm)
x (μm)
F
% agarose
0.125
0.25
0.5
1
G
LG
SI
H
LG SI

Figure 3

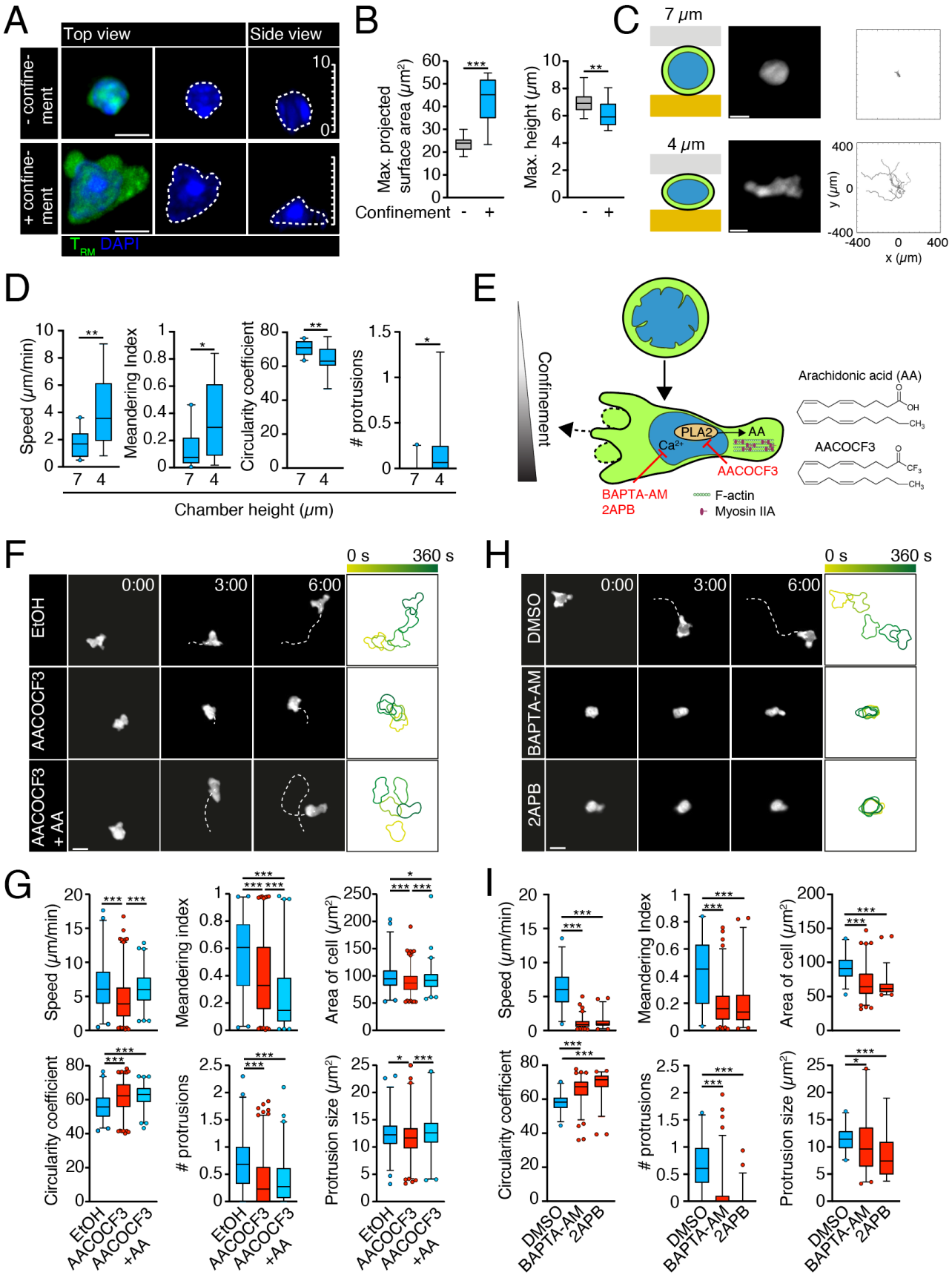
A
Top view
Side view
- confine-ment
+ confine-ment
10
0
T BM DAPI
B
Max. projected surface area (μm²)
Confinement - +
Max. height (μm)
C
7 μm
4 μm
y (μm)
x (μm)
D
Speed (μm/min)
Meandering Index
Circularity coefficient
protrusions
Chamber height (μm)
E
Confinement
Arachidonic acid (AA)
PLA2
AA
Ca2+
AACOCF3
BAPTA-AM
2APB
F-actin
Myosin IIA
F
0 s
360 s
EtOH
AACOCF3
AACOCF3 + AA
0:00
3:00
6:00
H
DMSO
BAPTA-AM
2APB
G
Speed (μm/min)
Meandering index
Area of cell (μm²)
Circularity coefficient
protrusions
Protrusion size (μm²)
EtOH
AACOCF3
AACOCF3 +AA
I
DMSO
BAPTA-AM
2APB

Figure 4

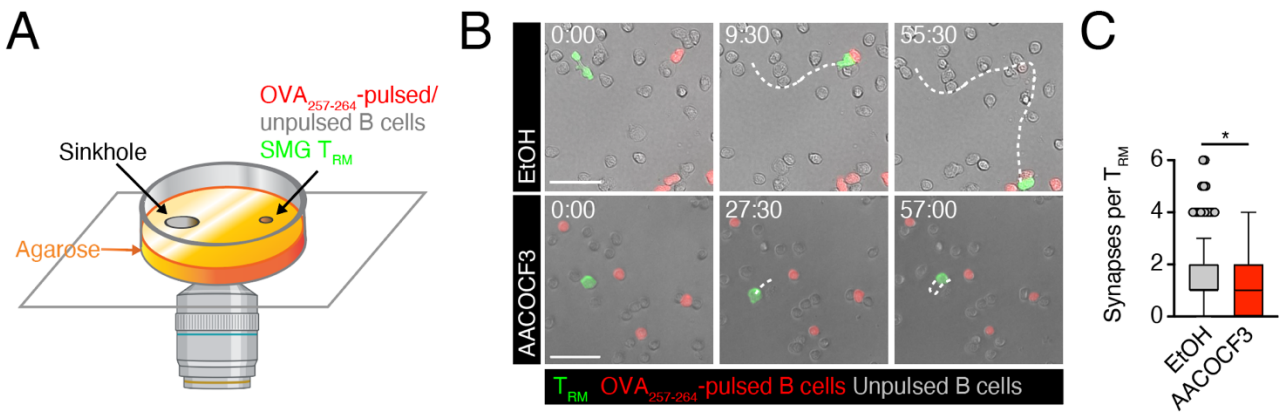

Figure 5

1208

1209

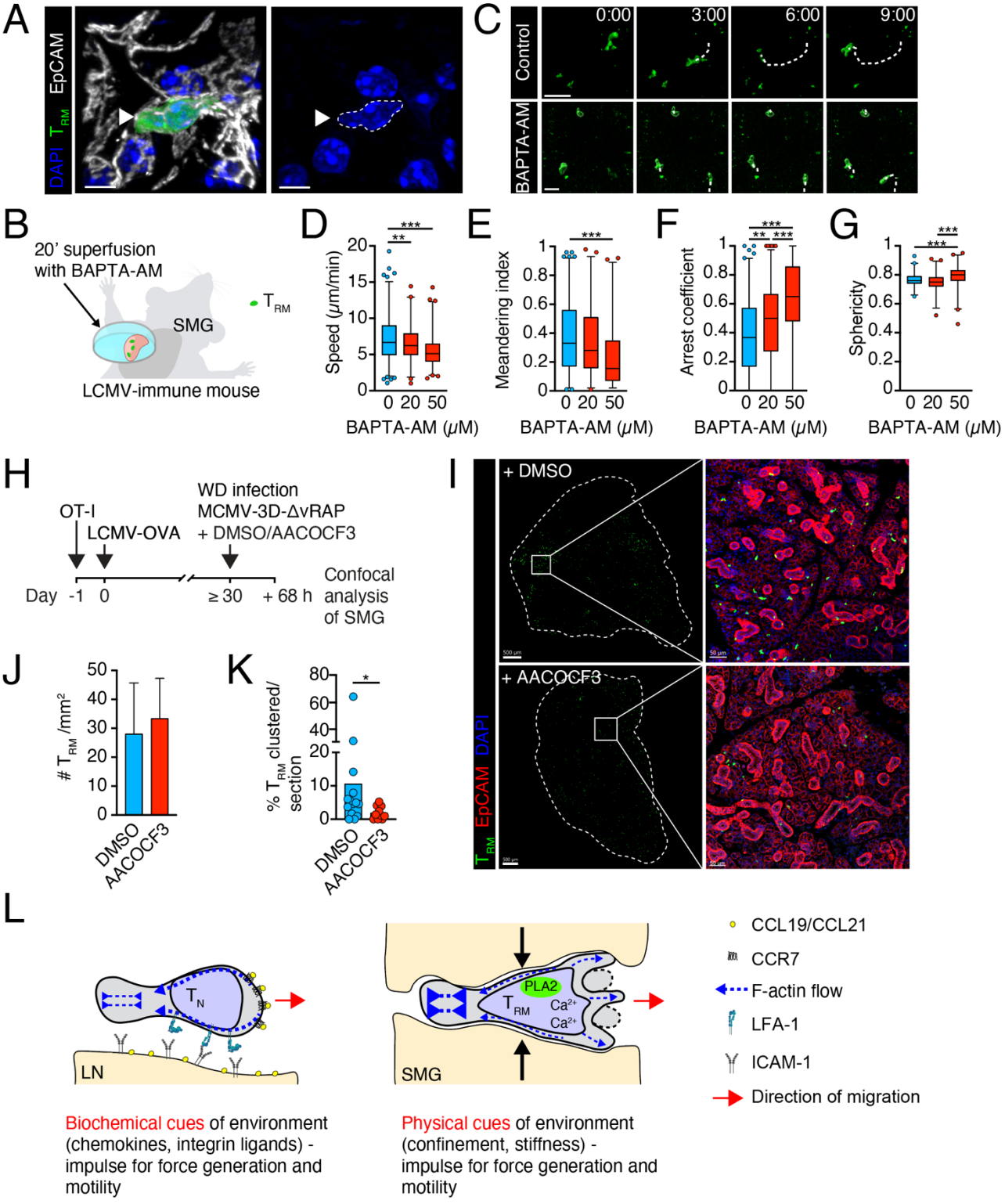
A
EpCAM
DAPI
C
Control
BAPTA-AM
0:00
3:00
6:00
9:00
B
20' superfusion
with BAPTA-AM
SMG
LCMV-immune mouse
D
Speed (μm/min)
E
Meandering index
F
Arrest coefficient
G
Sphericity
BAPTA-AM (μM)
H
OT-I
LCMV-OVA
WD infection
MCMV-3D-ΔvRAP
+ DMSO/AACOCF3
Day -1 0 ≥ 30 + 68 h
Confocal analysis of SMG
I
+ DMSO
+ AACOCF3
J
TRM /mm²
K
% TRM clustered/ section
DMSO
AACOCF3
L
TN
LN
PLA2
TRM
Ca2+
SMG
CCL19/CCL21
CCR7
F-actin flow
LFA-1
ICAM-1
Direction of migration
Biochemical cues of environment (chemokines, integrin ligands) - impulse for force generation and motility
Physical cues of environment (confinement, stiffness) - impulse for force generation and motility

Figure 6

Supplemental Material and Methods

CRISPR/Cas9-mediated MYH9 deletion in T cells

Myh9 crisprRNAs (crRNA) were designed using DESKGEN online tool (www.deskgen.com). Alt-R® CRISPR-Cas9 crRNA (custom design), trans-activator RNA (tracrRNA) (1072534) and Alt-R® CRISPR-Cas9 negative crRNA (226567203) were purchased from Integrated DNA Technologies (Coralville, IA, USA) and reconstituted at 100 µM with nuclease free duplex buffer (Integrated DNA Technologies). Nucleofection was performed as the following: One µL each of crRNA and tracrRNA were annealed to form gRNA at 95°C for 5 min using a thermal cycler and cooled to room temperature. Annealed gRNA was mixed with TrueCut Cas9 v2 (A36499, Thermo Fisher Scientific, Basel, Switzerland) at a ratio of gRNA : Cas9 = 1.8 µL : 1.2 µL (equivalent to 90 pmol : 36 pmol) and left at room temperature for > 10 min to generate RNP complex. Isolated naïve DsRed$^+$ MYH9-GFP$^+$ OT-I CD8$^+$ T cells were resuspended in Primary Cell 4D-Nucleofector™ X Kit S (Lonza, Basel, Switzerland) buffer solution at a cell concentration of 5 x 10^6 cells in 20 µL. The entire cell suspension was mixed with 3 µL per complex RNP solution and added to Nucleocuvette™ strip well. Cells were then nucleofected using a 4D-Nucleofector™ with X-Unit (V4XP-4032 and V4XP-9096, Lonza). Three RNP complexes in 9 µL were used per reaction. After nucleofection, 100 µL of pre-warmed complete medium containing 20 ng/mL recombinant mouse IL-7 was added to each Nucleocuvette™. Cells were gently mixed by pipetting and aliquoted into a flat-bottom 96-well plate. Cells were cultured in a total volume of 200 µL complete medium containing rmIL-7 at 2 x 10^6 CD8$^+$ T cells for 8-14 days at 37°C in a humidified 5% CO_2 atmosphere. The 3 crRNA sequences used in this study are listed below:

GCTGGTACTCACGAATCGAG
CATCTCGGCCAAGTATGCAG
CAAATACAAGGCCTCCATCG

NanoString analysis

Endogenous PI$^-$ CD44^{low} CD62L$^+$ CD8$^+$ T_N and PI$^-$ GFP$^+$ CD8$^+$ CD44^{high} CD62L$^+$ (= spleen OT-I T_{CM}) , PI$^-$ GFP$^+$ CD8$^+$ CD44^{high} CD62L$^-$ (= spleen OT-I T_{EM}) and PI$^-$ GFP$^+$ CD8$^+$ CD103$^+$ (= SMG T_{RM}) were sorted in triplicates and 4.5 x 10^4 cells of each lysed according to the manufacturer's

instructions (NanoString, UK). Lysates of were hybridized to a set of customized probes covering putative factors involved in migration and mechanosensing. The counts for each sample were normalized based on housekeeping gene expression.

Supplemental Figure legend

Figure S1. Flow cytometry of memory T cells. A. Gating strategy of spleen (pregated on lymphocyte FSC/SSC, singlets, $CD45^+/CD8^+$) and SMG (pregated on lymphocyte FSC/SSC, singlets, $CD45^+$) single cell suspensions of LCMV-OVA infected mice in memory phase. End., endogenous T cells. **B, C.** Flow cytometry analysis of T_N, T_{CM}, T_{EM} and SMG T_{RM} cell size (mean FSC, B) and normalized pCofillin levels (C). **D.** Flow cytometry analysis of DOCK2-GFP-expressing polyclonal $CD8^+$ T_{CM}, T_{EM} and SMG T_{RM} of LCMV-OVA infected mice in memory phase **E, F.** Flow cytometry analysis of T_N, T_{CM}, T_{EM} and SMG T_{RM} ERM (E) and pERM (F) levels. Data were pooled from at least two experiments (n = 9-12 mice) and analyzed by a Kruskal-Wallis test against LN T_N (B, C, E, F) or between all columns (D). *, $p < 0.05$; **, $p < 0.01$; ***, $p < 0.001$.

Figure S2. **Outline of morphometric analysis.** After determining the cell contour (1), cell trajectories are defined for motility parameters (2) together with local curvatures (3) to identify protrusions (4). The uropod is defined as the protrusion in the most opposite direction than the positive displacement of the cell (following its trajectory), and is excluded from the protrusion analysis. For more details, refer to the Material and Method section.

Figure S3. Autonomous SMG T_{RM} motility requires constitutive DOCK2-Rac-Arp2/3 signaling. A. Scheme of Arp2/3-mediated leading edge F-actin generation and selected inhibitors. **B.** DOCK2-GFP distribution in polarized T_{RM}. Quantification pooled from 7 cells, mean ± SEM. Scale bar, 10 µm. **C.** Wide-field fluorescence microscopy images of SMG T_{RM} under agarose migration in presence of CPYPP, CK666 and ML141. Time in min:s; Scale bar, 10 µm. **D.** Dynamic and morphometric analysis of SMG T_{RM} displacement. **E.** Wide-field fluorescence microscopy images of SMG T_{RM} under agarose migration in presence of W56 or control F56 peptide. Time in min:s; Scale bar, 10 µm. **F.** Dynamic and morphometric analysis of SMG T_{RM} displacement. **G.** Intravital image sequence of WT (white line) and $DOCK2^{-/-}$ SMG T_{RM} tracks (white dashed line). Time in min:s; Scale bar, 10 µm. **H, I.** Speeds and meandering index of WT and $DOCK2^{-/-}$ SMG (H) T_{RM} and $DOCK8^{-/-}$ SMG T_{RM} (I) assessed by 2PM. Data in D (n = 38-239 tracks), F (n = 155-363 tracks), H (n = 97-439 tracks) and I (n = 69-439 tracks) were pooled from at least two independent

experiments (except F: ML141, one exp. with n = 129 tracks) and analyzed by a Kruskal-Wallis test against control (D) or Mann-Whitney test (F, H, I). *, $p < 0.05$; **, $p < 0.01$; ***, $p < 0.001$.

Figure S4. Genetic depletion of MYH9 impairs T cell development and *in vivo* expansion. A. Flow cytometry analysis of MYH9 levels in control (wild type, WT) and CD4-cre x $MYH9^{fl/fl}$ OT-I T cells. Recovered peripheral T cells contained comparable MYH9 levels as non-deleted control cells using this early cre inducer model, suggesting thymic block of T cell development in absence of MYH9. **B.** Experimental layout of CRISPR/Cas9-mediated deletion of MYH9 in MYH-GFP reporter OT-I T cells and representative flow cytometry plot of control and MYH9-depleted OT-I T cells prior to adoptive transfer (n = 13 mice). Myosin IIA depletion is indicated by loss of GFP signal in MYH9-GFP OT-I T cells. RNP, Cas9 ribonuclein protein complex. **C.** Flow cytometry plots showing loss of MYH9-depleted OT-I T cells on day 6 p.i. with LCMV-OVA.

Figure S5. SMG T_{RM} motility requires Rho signaling. A-D. Under agarose SMG T_{RM} motility after inhibition of Rho (A, B) and Formins (F, G), and under agarose SMG T_{RM} motility with polystyrene beads + pluronic after inhibition of ROCK (C, D). Time in min:s; scale bar, 10 µm. **E.** Speeds and meandering index of control (baseline) and Y-27632-treated SMG containing WT T_{RM} determined by 2PM. **F, G.** Under agarose SMG T_{RM} motility after inhibition of Formins. Data in D (n = 37-92 tracks) and E (n = 102-133 tracks) were pooled from two experiments (except B: one exp. with n = 52-98 tracks) and analyzed by a Mann-Whitney test. *, $p < 0.05$; **, $p < 0.01$; ***, $p < 0.001$.

Figure S6. T cell motility under confinement. A. Speeds and cell area of T_{RM} and T_N in 4 and 2-µm high chambers. **B.** Example of T_{RM} membrane rupture (arrowhead) in a 2 µm-high confinement chamber. Time in min:s; scale bar, 10 µm. **C.** Speeds and meandering index of T_N under agarose on ICAM-1 in presence or absence of AA, CCL21 and AACOCF3. **D.** Speeds and meandering index of T_{RM} under agarose on ICAM-1 and CXCL10 ± AACOCF3. Data in A (n = 25-89 tracks) and C (n = 142-609 tracks) are pooled from 2 independent experiments and analyzed using ANOVA with Sidak's multiple comparison test (speeds) or Kruskal-Wallis (meandering index). Data in D is

from one experiment (n = 18-40 tracks) and analyzed by unpaired t-test (speeds) and Mann-Whitney (meandering index). *, $p < 0.05$; ***, $p < 0.001$.

Figure S7. Gene expression analysis. A, B. Expression of *Pla2g4a* in T cell subsets in Immgen database (A; shown as robust multichip normalization, RMA) and qPCR (B). DN, double negative thymocytes. **C.** Nanostring analysis of subset-specific marker expression in sorted OT-I T_N, T_{CM}, T_{EM} and T_{RM}. **D-G**. Nanostring expression analysis of *Pla2g* isoforms (D), InsP3R-encoding genes (E), nuclear cytoskeleton components (F) and nuclear-cytoplasmic anchoring components (G) in T_N, T_{CM}, T_{EM} and T_{RM}.

Figure S8. Characterization of SMG viral rechallenge experiment and inhibitors. A, B. Speeds (A) and meandering index (B) of T_{RM} before (n = 386 tracks) and 1-4 h after administration of AACOCF3 (n = 924 tracks) determined by 2PM. **C.** Exemplary flow cytometry plot of CD69 and CD103 staining on SMG T_{RM}. **D.** Quantification of SMG T_{RM} numbers at 3 d of DMSO or AACOCF3 treatment in presence or absence of anti-α4 and anti-LFA-1 (α_L) mAb block (n = 3-5 mice from 2 independent experiments). Bars depict mean ± SD. **E.** Experimental layout of Wharton's duct infection for MCMV-3D-ΔvRAP rechallenge into one SMG lobe and example image of TRITC-dextran injection. Line marks outline of SMG lobes. **F.** T_{RM} numbers in uninfected (blue) and contralaterally infected (dark red) SMG lobes from one of two independent experiments (n = 3 mice per condition). **G.** Percentage of blood $CD3^+$ following FTY720 treatment (n = 8 mice from 2 independent experiments). Bars depict mean ± SD. **H.** Confocal SMG section depicting a rare $mCherry^+$ MCMV-infected cell (arrowhead) in SMG at 68 h p.i. Scale bar, 50 µm. Right plot depicts number of $mCherry^+$ viral foci per area (n = 4 sections from one experiment). Data in A, G and H were analyzed with an unpaired t-test and data in B with a Mann-Whitney test. Data in D were analyzed using ANOVA. **, $p < 0.01$; ***, $p < 0.001$.

Supplementary movie legend

Movie 1. Intravital imaging of OT-I T_{RM} migration in SMG during the memory phase following LCMV-OVA infection. SHG, second harmonic generation. Time in min:s. Image sequence recorded using the LaVision Biotec TrimScope system.

Movie 2. TIRF time-lapse video of F-actin dynamics in LifeAct-GFP$^+$ OT-I T_N in under agarose assay. Time in min:s. Image sequence recorded using the DeltaVision system.

Movie 3. TIRF time-lapse video of F-actin dynamics in LifeAct-GFP$^+$ SMG OT-I T_{RM} in under agarose assay. Time in min:s. Image sequence recorded using the DeltaVision system.

Movie 4. Widefield fluorescent microscopy time-lapse video of OT-I T_N in under agarose assay on HSA or CCL19 and ICAM-1. Time in min:s. Image sequence recorded using the DeltaVision system.

Movie 5. Widefield fluorescent microscopy time-lapse video of SMG OT-I T_{RM} in under agarose assay on HSA or CXCL10, CXCL10 and ICAM-1. Time in min:s. Image sequence recorded using the DeltaVision system.

Movie 6. Widefield fluorescent microscopy time-lapse video of SMG OT-I T_{RM} in under agarose assay on HSA and CPYPP or CK666. Time in min:s. Image sequence recorded using the DeltaVision system.

Movie 7. Intravital imaging of DOCK2$^{-/-}$ and WT OT-I T_{RM} in SMG during the memory phase following LCMV-OVA infection. SHG, second harmonic generation. Time in min:s. Image sequence recorded using the LaVision Biotec TrimScope system.

Movie 8. Widefield fluorescent microscopy time-lapse video of DsRed$^+$ MYH-GFP$^+$ SMG OT-I T_{RM} in under agarose assay on HSA. Time in min:s. Image sequence recorded using the DeltaVision system.

Movie 9. Widefield fluorescent microscopy time-lapse video of SMG OT-I T_{RM} in under agarose assay on HSA and MLCK or Y-27632. Time in min:s. Image sequence recorded using the DeltaVision system.

Movie 10. Widefield fluorescent microscopy time-lapse video of mT/mG$^+$ LifeAct-GFP$^+$ or DOCK2-GFP$^+$ SMG OT-I T_{RM} in under agarose assay, followed by confocal microscopy time-

lapse image sequence of mT/mG$^+$ LifeAct-GFP$^+$ SMG OT-I T_{RM} in 3D collagen matrix. Time in min:s. Image sequence recorded using the DeltaVision or Leica confocal imaging system.

Movie 11. Widefield fluorescent microscopy time-lapse video of SMG OT-I T_{RM} in confinement chamber with micropillars of 7 µm or 4 µm height. Time in min:s. Image sequence recorded using the DeltaVision system.

Movie 12. Widefield fluorescent microscopy time-lapse video of SMG OT-I T_{RM} in under agarose assay on HSA with EtOH, AACOCF$_3$ and AACOCF$_3$ + AA. Time in min:s. Image sequence recorded using the DeltaVision system.

Movie 13. Widefield fluorescent microscopy time-lapse video of SMG OT-I T_{RM} in under agarose assay on HSA with DMSO, BAPTA-AM and 2APB. Time in min:s. Image sequence recorded using the DeltaVision system.

Movie 14. Widefield fluorescent microscopy time-lapse video of SMG OT-I T_{RM} in under agarose assay on HSA with OVA$_{257-264}$-pulsed and unpulsed B cells with or without AACOCF$_3$. Scale bar, 10 µm; time in min:s. Image sequence recorded using the DeltaVision system.

Movie 15. Intravital imaging of SMG T_{RM} before and after BAPTA-AM (50 µM) superfusion. Scale bar, 20 µm. Time in min:s. Image sequence recorded using the LaVision Biotec TrimScope system.

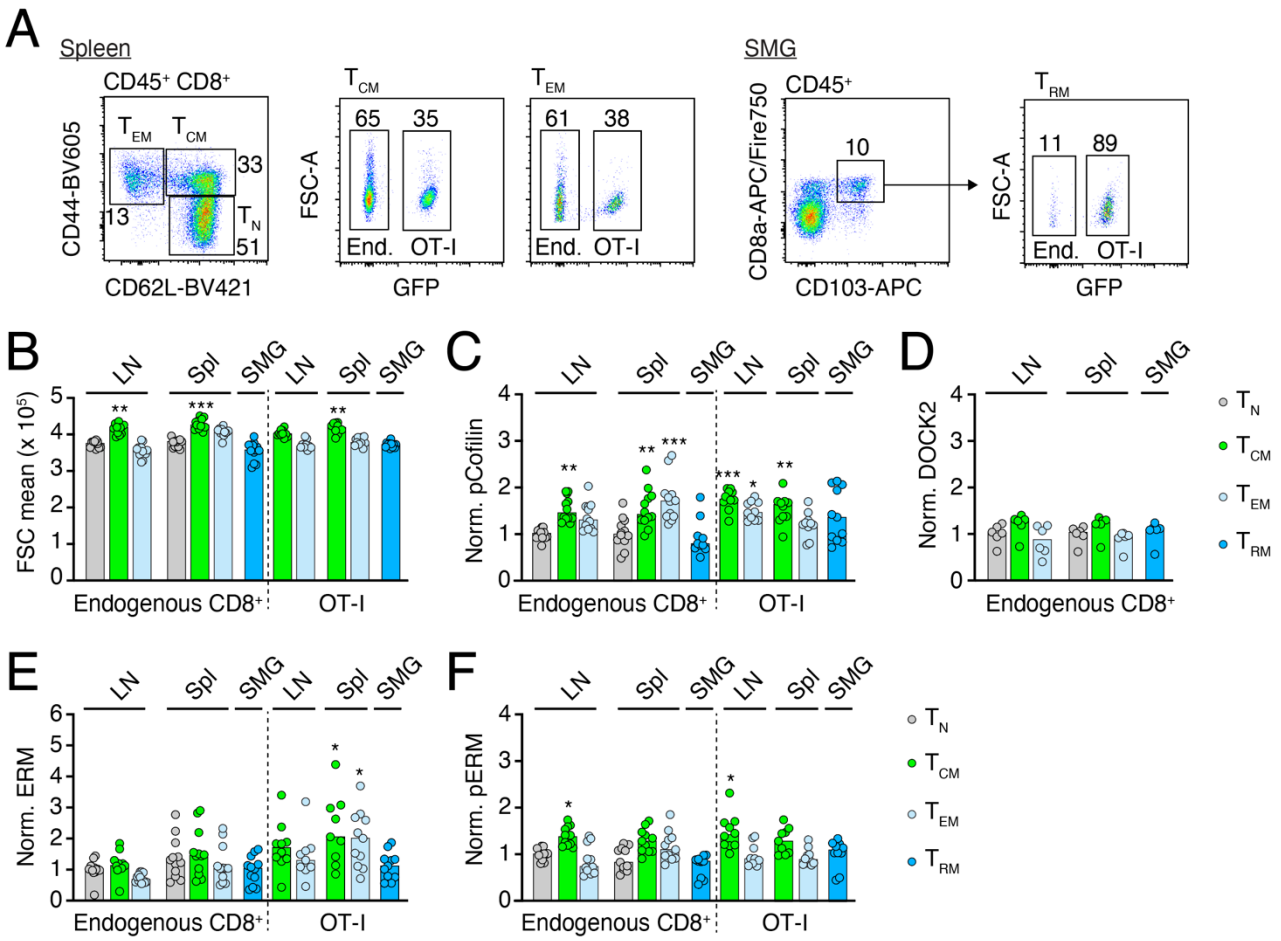
A
Spleen
CD45+ CD8+
TEM TCM
33
13
TN
51
CD44-BV605
CD62L-BV421
TCM
65 35
End. OT-I
FSC-A
GFP
TEM
61 38
End. OT-I
SMG
CD45+
10
CD8a-APC/Fire750
CD103-APC
TRM
11 89
End. OT-I
FSC-A
GFP
B
FSC mean (x 10⁵)
LN Spl SMG LN Spl SMG
Endogenous CD8+
OT-I
C
Norm. pCofilin
LN Spl SMG LN Spl SMG
Endogenous CD8+
OT-I
D
Norm. DOCK2
LN Spl SMG
Endogenous CD8+
TN
TCM
TEM
TRM
E
Norm. ERM
LN Spl SMG LN Spl SMG
Endogenous CD8+
OT-I
F
Norm. pERM
LN Spl SMG LN Spl SMG
Endogenous CD8+
OT-I
TN
TCM
TEM
TRM

Figure S1

1.Determining
cell contour

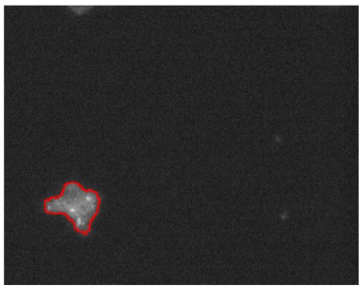

2. Forming cell trajectories
to determine displacement direction

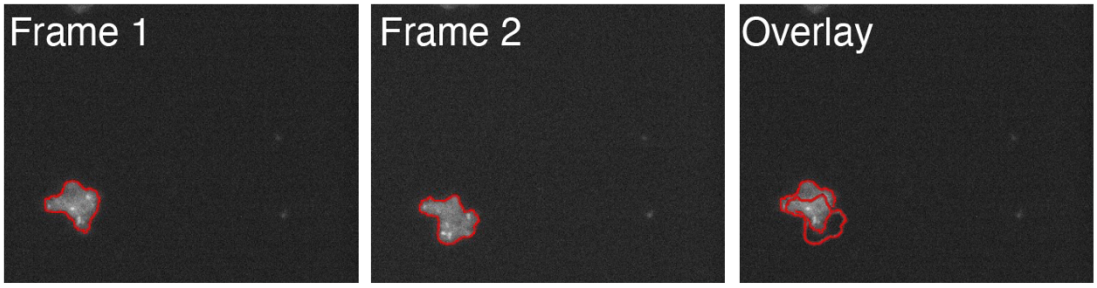

3. Calculating
local curvatures

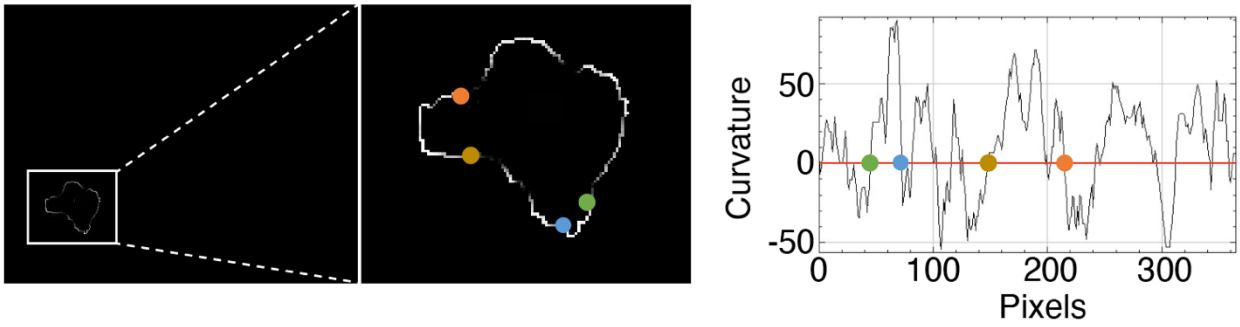

4. Defining
the protrusions

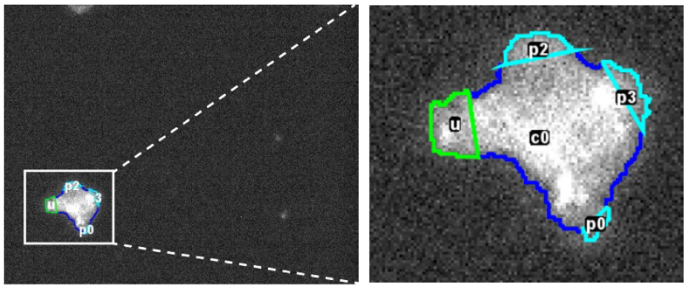

u = uropod

p = protrusion

Figure S2

1374

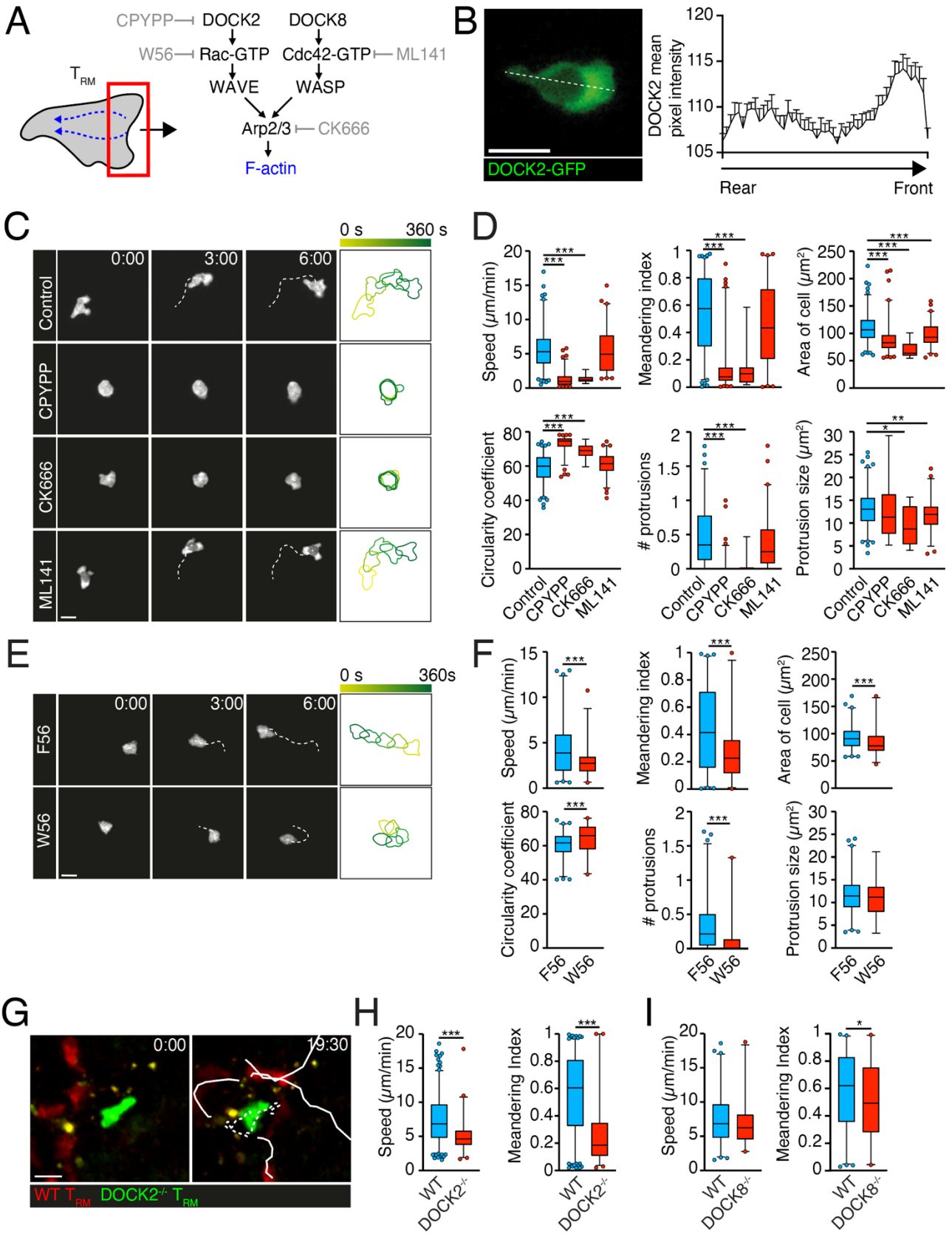
A
CPYPP
DOCK2
DOCK8
W56
Rac-GTP
Cdc42-GTP
ML141
WAVE
WASP
Arp2/3
CK666
F-actin
T RM
B
DOCK2-GFP
DOCK2 mean pixel intensity
120
115
110
105
Rear
Front
C
0 s
360 s
0:00
3:00
6:00
Control
CPYPP
CK666
ML141
D
Speed (μm/min)
Meandering index
Area of cell (μm²)
Circularity coefficient
protrusions
Protrusion size (μm²)
Control
CPYPP
CK666
ML141
E
0 s
360s
F56
W56
F
F56
W56
G
0:00
19:30
WT T RM
DOCK2-/- T RM
H
Speed (μm/min)
Meandering Index
WT
DOCK2-/-
I
DOCK8-/-

Figure S3

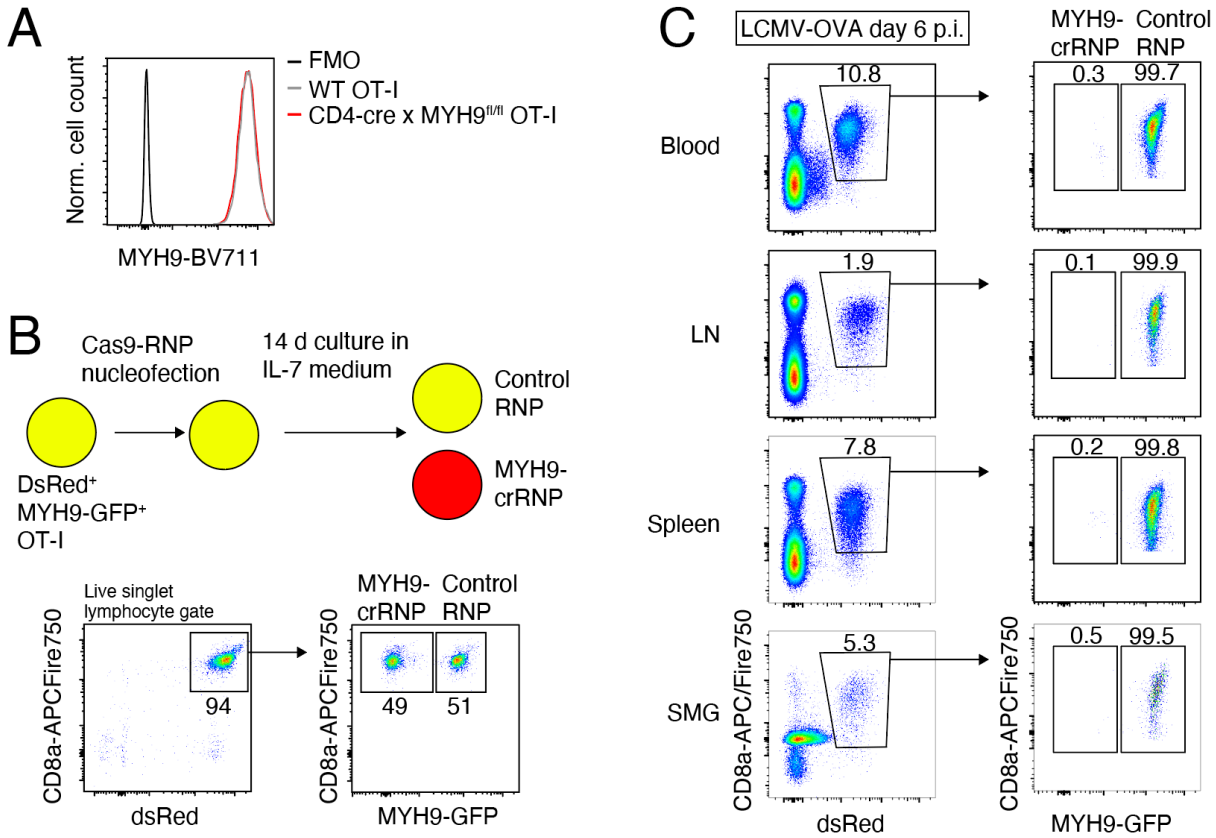

Figure S4

1376

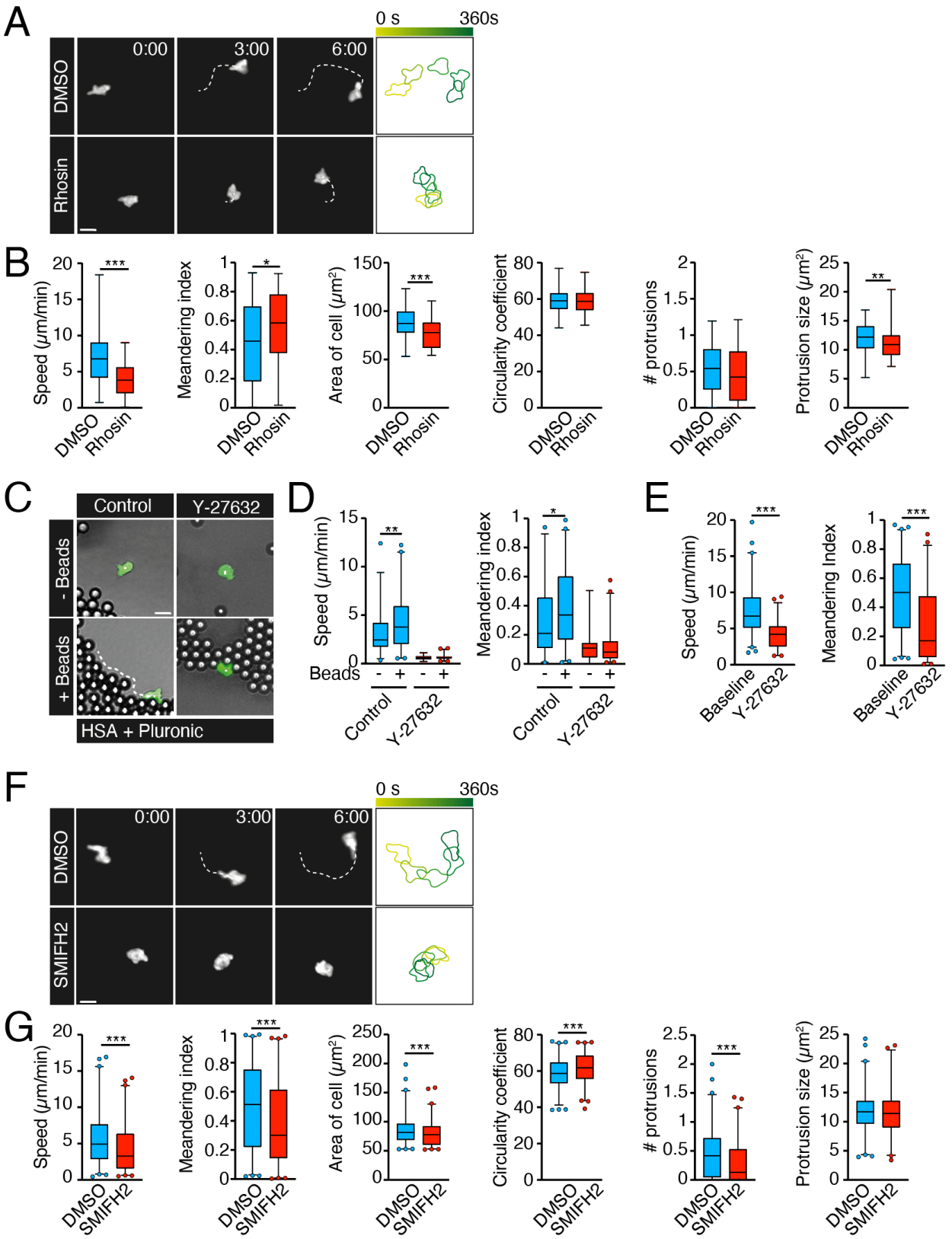
A
0 s
360s
0:00
3:00
6:00
DMSO
Rhosin
B
Speed (μm/min)
Meandering index
Area of cell (μm²)
Circularity coefficient
protrusions
Protrusion size (μm²)
DMSO
Rhosin
C
Control
Y-27632
- Beads
+ Beads
HSA + Pluronic
D
Speed (μm/min)
Meandering index
Beads
Control
Y-27632
E
Speed (μm/min)
Meandering Index
Baseline
Y-27632
F
SMIFH2
G

Figure S5

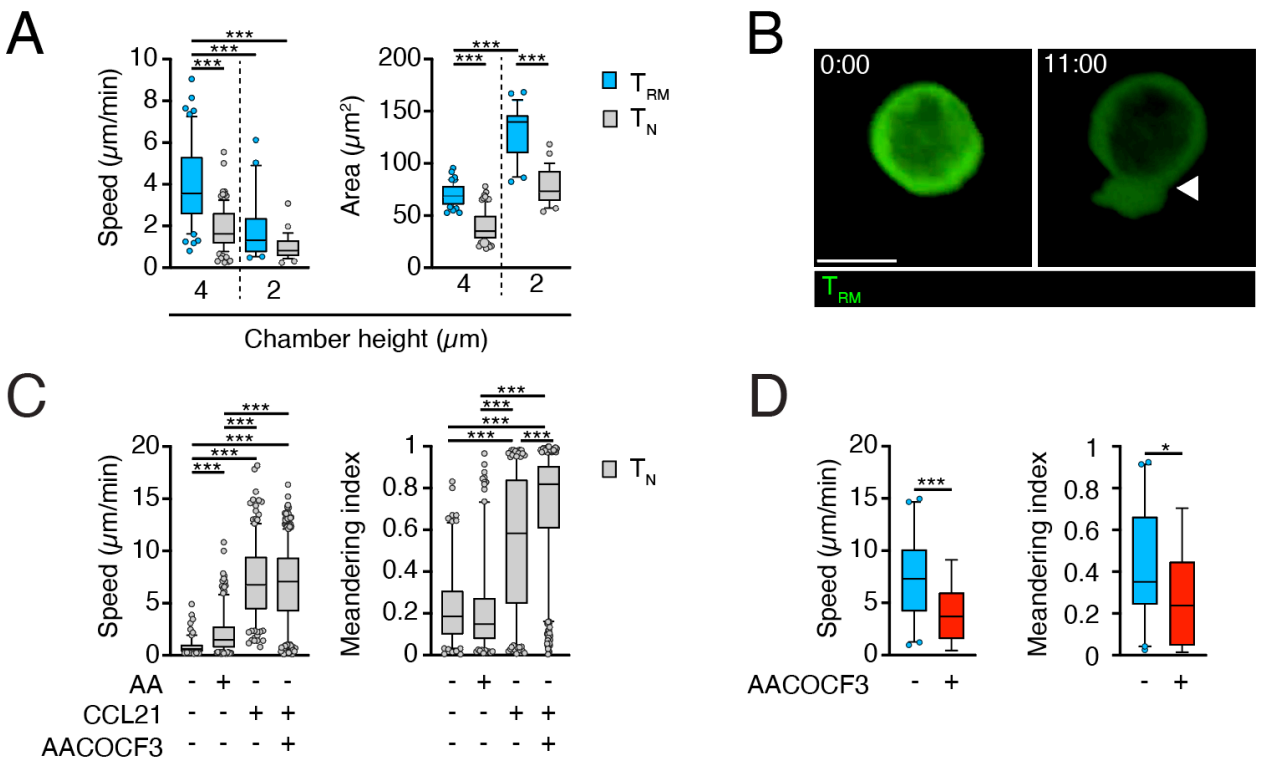
A
Speed (μm/min)
Area (μm²)
Chamber height (μm)
T_RM
T_N
B
0:00
11:00
T_RM
C
Speed (μm/min)
Meandering index
AA
CCL21
AACOCF3
D
Speed (μm/min)
Meandering index
AACOCF3

Figure S6

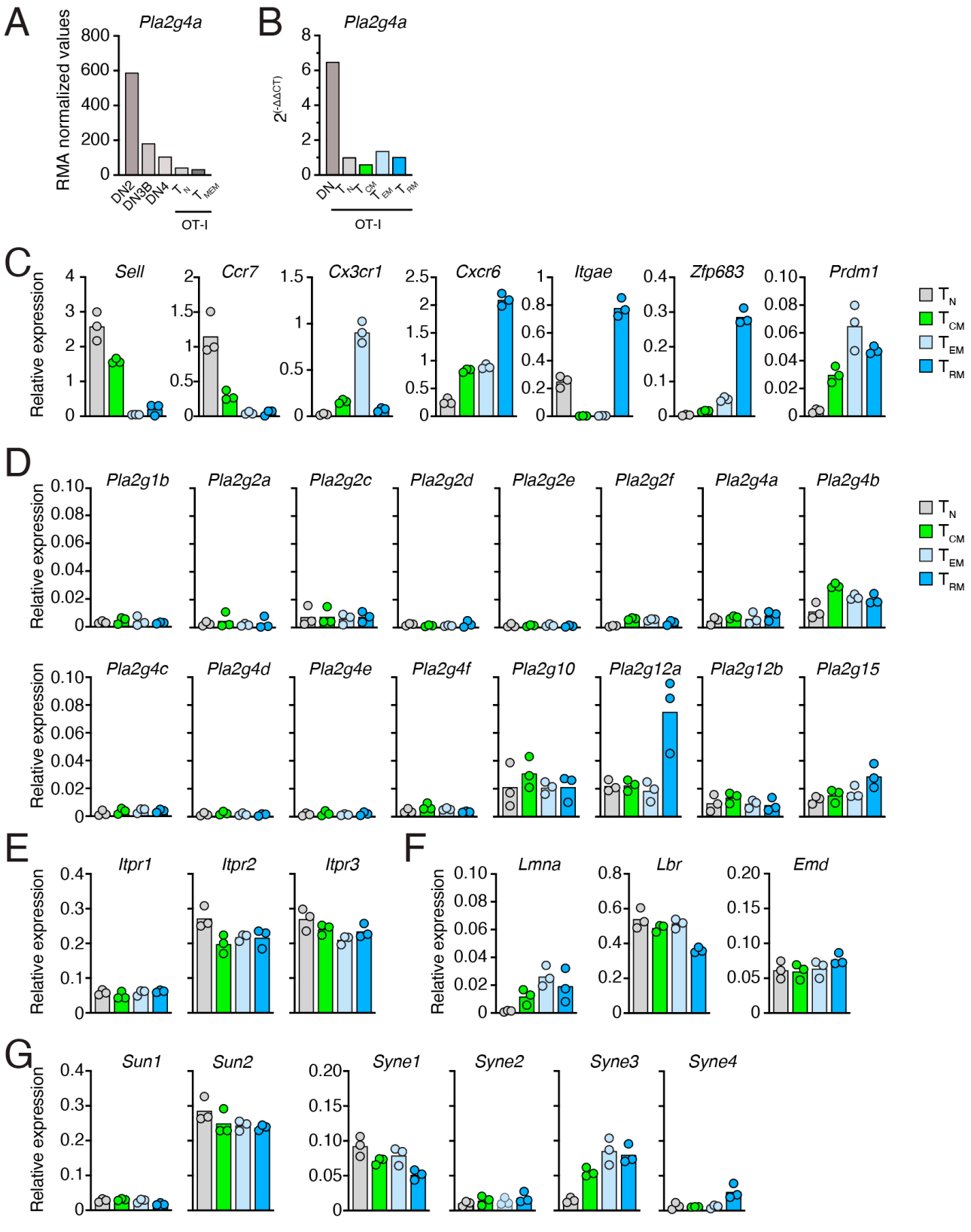
A
Pla2g4a
RMA normalized values
800
600
400
200
0
DN2
DN3B
DN4
T N
T MEM
OT-I
B
Pla2g4a
2(-ΔΔCT)
8
6
4
2
0
DN
T N
T CM
T EM
T RM
OT-I
C
Sell
Ccr7
Cx3cr1
Cxcr6
Itgae
Zfp683
Prdm1
Relative expression
T N
T CM
T EM
T RM
D
Pla2g1b
Pla2g2a
Pla2g2c
Pla2g2d
Pla2g2e
Pla2g2f
Pla2g4a
Pla2g4b
Pla2g4c
Pla2g4d
Pla2g4e
Pla2g4f
Pla2g10
Pla2g12a
Pla2g12b
Pla2g15
Relative expression
E
Itpr1
Itpr2
Itpr3
F
Lmna
Lbr
Emd
G
Sun1
Sun2
Syne1
Syne2
Syne3
Syne4

Figure S7

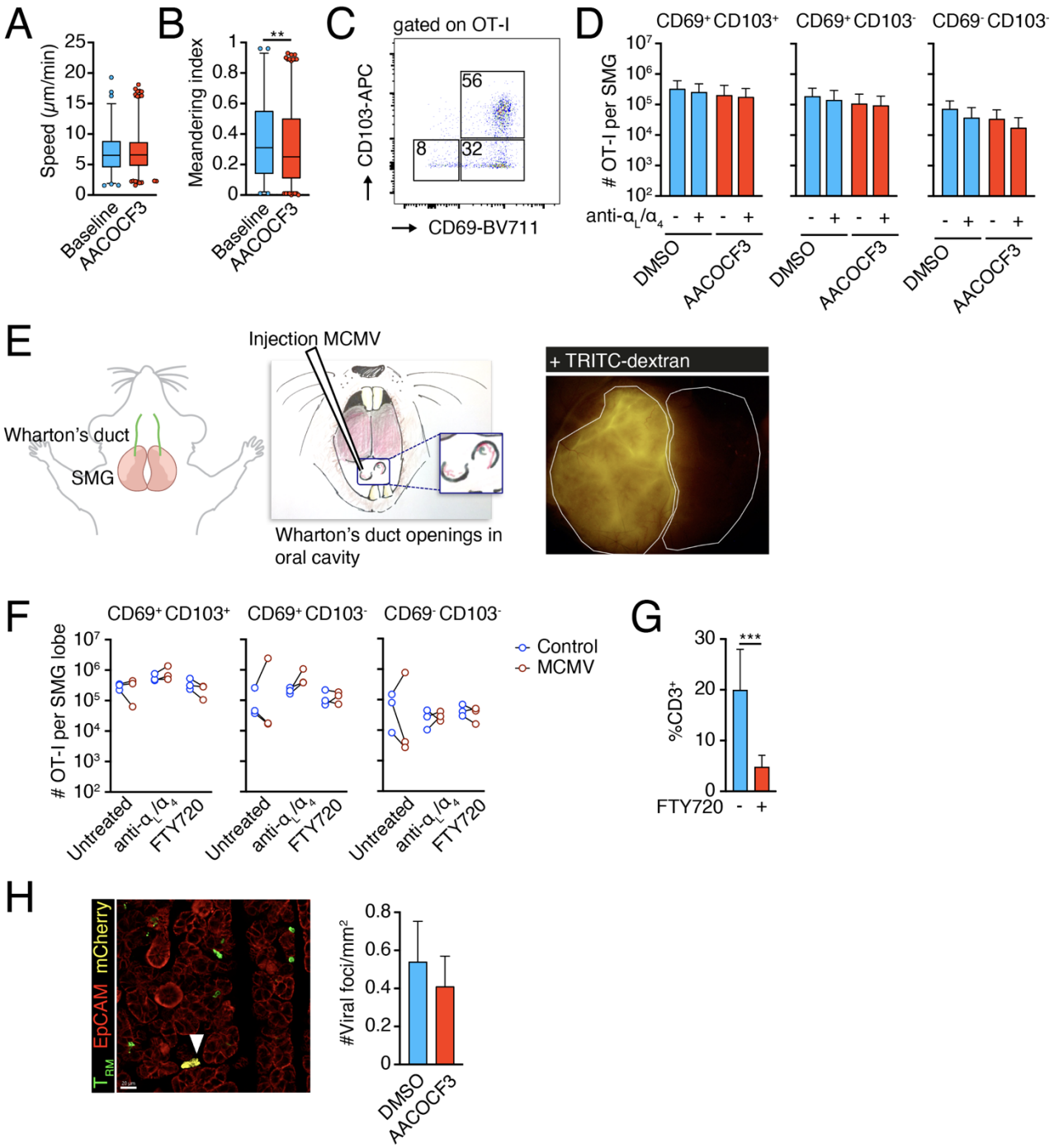

Figure S8

1383